RAB14-dependent tubulovesicular recycling directs MET to invadopodia promoting TNBC cell invasion.

Amrita Khamari[1], Atreyee Guria[1], Kiran Tak[1], Rajiv Sharma[2], Yannis Kalaidzidis[3] & Sunando Datta[1]

[1] Department of Biological Sciences, Indian Institute of Science Education and Research, Bhopal, Bhopal-462066, India.

[2] Indian Institute of Technology, Delhi, India

[3] Max Planck Institute of Molecular Cell Biology and Genetics, Dresden, Germany.

*Corresponding Author

Email Address: sunando@iiserb.ac.in

ABSTRACT

Metastasis is one of the primary causes of cancer-related death in TNBC patients. During metastasis, stromal infiltration requires the cancer cells to form invadopodia, a membrane-protrusion with proteolytic activity. Cues from growth factors via the cognate RTKs promote invadopodia formation and cancer cell invasion. This study demonstrated the role of the HGF-MET axis in invadopodia formation and associated protease trafficking. MET interacts with MT1-MMP and is co-transported to the cell surface. Further, the RTK is found to reside at invadopodia, and its recruitment increases upon HGF stimulation due to enhanced recycling mediated by RAB4 and RAB14. The study further highlights the role of RCP in MET recycling by bringing RAB14 and MET together onto endosomal subdomains. KIF16B, a molecular motor, gets recruited to MET-containing endosomes via RAB14 and promotes the endosomal tubulation, which could be crucial for MET recycling.

Collectively, the study provides new insights into the mechanism of tubulovesicular recycling of MET and its implications in cancer cell invasion.

INTRODUCTION

Triple-negative breast cancer is a highly aggressive subtype of breast cancer and is characterized by the lack of expression of three key receptors: estrogen receptor (ER), progesterone receptor (PR), and human epidermal growth factor receptor 2 (HER2), which are generally targeted in conventional breast cancer therapies. The absence of these hormonal receptors in TNBCs imposes challenges in the treatment. Metastasis is one of the leading causes of TNBC patient morbidity and mortality (1). Metastasis requires the tumor cells to cross the tissue barrier, migrate to a distant organ through circulation and colonize to form a secondary tumor (1). To cross the tissue boundary, cancer cells navigate through the collagen-rich extracellular matrix (ECM) meshwork, employing either amoeboid movement or protease-dependent migration. The space within the collagen network, nuclear deformability, and positioning are the key deciding factors for the cancer cells to migrate in a protease-dependent or independent manner (2,3). Invadopodia, an actin-rich membrane protrusion decorated with proteases, is a tool for ECM and basement membrane degradation during cancer cell invasion (4).

The biogenesis of Invadopodia can be accomplished in four stages (5). The initiation involves the formation of an invadopodia precursor comprised of actin and its modulators, which further gets anchored to the plasma membrane through TKS5. Next, the actin polymerizes to form a membrane protrusion, to which proteases like MT1-MMP, MMP2, and MMP9 are delivered in a regulated fashion for invadopodia maturation (6,7). The role of invadopodia in TNBCs is indispensable. Studies suggest that the invasive cells in the leading front form invadopodia to create micro-tracks for the follower cells (8). Growth factors and their receptors, including EGF-EGFR and HGF-MET, can modulate the invadopodia-associated molecules, thereby promoting invadopodia-associated cancer invasion and metastasis (9–12).

Amplification of EGFR and MET in TNBC is associated with poor prognosis, yet they pose as potential targets for its treatment (13,14). At the cell surface, the RTKs bind to their respective ligands, leading to receptor dimerization and activation. Subsequently, they internalize rapidly and continue to signal from endosomes (15). Signaling cues from RTKs are essential for invadopodia formation and ECM remodelling (11,16). TPRMET, an oncogenic variant of MET, forms invadopodia structures in fibroblast cells (11). Similarly, EGFR overexpression promoted invadopodia formation in melanoma cells (17). SNARE-dependent delivery of EGFR to invadopodia promotes invadopodia-associated tumor

invasion, highlighting the potential role of RTK trafficking in cancer cell invasion (10). EGFR induces Cortactin phosphorylation through SRC and ARG, which triggers invadopodia formation (9). However, MET-directed Cortactin phosphorylation in invadopodia is SRC or ARG-independent, indicating the differential function of MET in invadopodia formation (11). Though MET is known to be involved in invadopodia-associated cancer invasion, the detailed mechanisms are yet to be explored.

Here, we investigated the role of HGF and its cognate receptor, MET, in invadopodia-associated cancer cell invasion in TNBC cell lines. Our study revealed that activated MET resides at invadopodia and its invadopodia-recruitment is enhanced upon HGF stimulation. Our findings emphasize the importance of the growth factor-mediated cell-surface transport of MET in invadopodia formation and MT1-MMP recruitment through physical interaction with the protease that leads to enhanced TNBC invasion upon HGF stimulation. We further delineated the involvement of the cellular recycling repertoire in the growth factor-stimulated recycling of MET.

RESULTS

HGF-induced MET activity promotes TNBC breast cancer invasion through invadopodia-mediated ECM degradation

The upregulation of EGFR and MET promotes breast cancer invasion (18,19). To understand the correlation between gene alteration in these RTKs and the outcome of invasive breast cancer, we analyzed 14155 samples in 27 breast cancer datasets using cBioportal (https://www.cbioportal.org/). MET was found to be altered in 2% of the breast cancer samples (Fig. S1A). Next, the correlation between gene alteration of EGFR or MET and patient survival was inspected and found to be negatively correlated with the survival of the patients (Fig. S1B).

MET, upon activation by HGF, triggers the activation of the RTK that induces cancer cell invasion (12,20). We examined the MET expression in TNBC cell lines MDA-MB-231, BT-549, and the non-TNBC invasive breast cancer cell line MCF10A DCIS by immunoblotting. We observed comparable MET expression in all 3 cell lines (Fig. S1C). Next, to inspect the effect of HGF on the invasive properties of breast cancer cell lines, we employed a spheroid invasion assay that closely resembles the physiological environment. Spheroids were formed using MDA-MB-231 or BT-549 cells and embedded in collagen I with or without HGF or in complete media. The spheroids were allowed to invade for 48 hours. The ratio of core area to

invaded area was calculated, revealing that HGF-treated cells invaded more into collagen compared to untreated conditions (Fig. 1A, S1D, MOVIE 1).

To invade the stroma, tumor cells degrade the underlying basement membrane. To understand the effect of HGF on ECM remodelling, we carried out a fluorescent-labelled gelatin degradation assay. We seeded cells on Alexa568-labeled gelatin-coated coverslips in the presence or absence of HGF and allowed them to degrade gelatin for a minimum of three hours. The loss of fluorescence due to gelatin degradation, represented as the degradation index, was calculated as detailed in the methods section. Our results showed that HGF treatment significantly increased gelatin degradation activity in MDA-MB-231, BT-549, and MCF10A DCIS cell lines (Fig. 1B, S1E, F).

The ECM degradation activity of cancer cells is attributed to invadopodia formation (5,21). Therefore, we investigated the ability of HGF to induce invadopodia formation. Cells were seeded on gelatin in the presence or absence of HGF for 6h, fixed, and immunostained for known invadopodia markers, i.e., TKS5, Cortactin, or Actin. Puncta positive for two invadopodia markers were considered as invadopodia. When stimulated with HGF, increased numbers of invadopodia were observed in MDA-MB-231, BT-549 and MCF10A DCIS cells (Fig. 1C, S1E, G). Additionally, the other most abundant RTK in TNBC cells, EGFR, when activated by EGF, resulted in a significant increase in invadopodia number in MDA-MB-231 (Fig. S1H) cells, corroborating previous studies (9).

Next, to study whether MET activation is essential for invadopodia formation, we inhibited the kinase activity of MET using the drug PHA665752. Immunoblot analysis revealed that HGF stimulation increased MET pTyr1234-1235 (pY-MET), which was abolished by the drug (Fig. S1J). Interestingly, the drug treatment also led to degradation of MET (Fig. S1J). MDA-MB-231 cells were analyzed for their ability to form invadopodia in the presence of 5 μM of the drug or vehicle, with or without HGF. Inhibition of MET kinase activity using PHA665752 abolished the HGF-induced invadopodia formation (Fig. 1D, E).

To investigate whether MET is important for HGF-governed invadopodia formation, MET was silenced using different clones of shRNA against MET, and the level of silencing was evaluated (Fig. S1I). MDA-MB-231 cells were transfected with control SHC002 or MET shRNA C#3. After 36h, cells were seeded on labelled gelatin for 6h, fixed, and immunostained with phalloidin and an antibody against MET. Invadopodia formation was abrogated in the MET-depleted cells compared to the control (Fig. 1F, S1I).

Taken together, HGF activates RTK MET and promotes TNBC invasion by enhancing invadopodia formation and associated activity.

Enhanced MET recruitment to Invadopodia upon HGF stimulation

Since MET activity was found to be important for invadopodia formation, we first asked if MET is localized at invadopodia. MDA-MB-231 cells were seeded on a gelatin-coated surface for 6 hours. Then, the cells were fixed and immunostained for MET and Cortactin. A notable population of Cortactin puncta was found to be localized with MET (Fig. 2A). Next, the colocalization of MET to GFP-TKS5 was examined using TIRF microscopy (TIRFM). Approximately 30% of the TKS5 population showed staining for MET (Fig. 2B, D). Confocal imaging of BT-549 cells immunostained for TKS5 and MET revealed that MET-TKS5 colocalization follows the same trend as MDA-MB-231 (Fig. S2A). Next, we asked whether MET is in its active form at invadopodia. Cherry-TKS5 expressing cells were seeded on gelatin, fixed, and immunostained for phosphorylated pY-MET. TIRF imaging revealed that 27% of TKS5 puncta are positive for pY-MET, similar to that of MET localization to TKS5-positive invadopodia (Fig. 2C, D).

TKS5 is a critical component of invadopodia and its concentration gradually increases as the invadopodia matures (22). When we plotted the normalized steady-state fluorescence intensity of MET and TKS5 localized at invadopodia, the resulting plot showed two different populations of invadopodia. Invadopodia with TKS5 intensity less than 4 showed no correlation with MET intensity ($R^2 = 0.03$ for linear regression); however, Invadopodia with TKS5 intensity more than 4 showed a negative correlation ($R^2 = 0.3$ for linear regression) (Fig. 2E). Further, we analyzed the frequency distribution of the MET to TKS5 fluorescence intensity ratio across invadopodia. It revealed that most invadopodia structures exhibited lower MET/TKS5 ratios (Fig. S2B). This observation prompted us to investigate the apparent absence of MET from mature invadopodia. To address this, the localization of MET at the invadopodia-mediated degradation spots was examined in the MDA-MB-231 cells plated on fluorescence-labelled gelatin. As implied above, the degradation spots did not show strong colocalization with MET (Fig. 2F).

As we have observed that HGF stimulates invadopodia formation via MET and the RTK is physically localized at the invadopodia site, we asked if HGF influences MET localization to the invadopodia. Cells were seeded on gelatin with or without HGF, fixed, and immunostained for MET and invadopodia markers. Intriguingly, upon treatment with HGF, we observed an

increased MET-containing TKS5-positive invadopodia structure in both MDA-MB-231 and BT-549 (Fig. 2G, S2C, D). This observation led us to hypothesize that HGF may induce the surface delivery of MET to invadopodia.

Previously, it was reported that HGF stimulation leads to endocytosis of MET, followed by lysosomal degradation of the RTK (23,24). First, we analyzed the effect of HGF on receptor endocytosis and degradation of MET. To study the HGF-mediated receptor endocytosis, the colocalization of MET with RAB5 was quantified with or without HGF. The percent colocalization of MET with RAB5 was found to be increased from 12% to 43% in the presence of HGF stimulation (Fig. S2E). Next, cells were incubated with HGF for different time points, and the total MET levels were quantified using immunoblotting. After 3h of HGF stimulation, ~50% of MET was found to be degraded (Fig. S2F). To validate our hypothesis that HGF can induce surface delivery of MET, GFP-MET-expressing cells were imaged with TIRFM with or without HGF, and MET tracks were quantified as explained in the method. In the presence of HGF, an increased number of MET tracks were found near the plasma membrane compared to the untreated cells (Fig. 2H, MOVIE 2). This suggests that HGF indeed increases the trafficking of MET to the cell surface. We also observed a similar effect of EGF on EGFR localization at invadopodia (Fig. S2G, H), consistent with an earlier study in MDA-MB-231 (10).

These observations convey that MET resides in the invadopodia structures and HGF treatment leads to enhanced surface delivery of MET and its recruitment to invadopodia.

HGF-mediated surface delivery of MET promotes invadopodia-associated ECM degradation and breast cancer cell invasion

As HGF promotes MET recycling and breast cancer invasion, we investigated whether MET recycling drives invadopodia-associated TNBC invasion. To address this, we employed the degradation-defective M1250T mutant and the endocytosis-defective LL/AA MET mutant as a negative control. An oncogenic mutation in MET at M1268T (M1250 in the MET constructs used in this study) is naturally found in papillary renal carcinoma, has a degradation defect leading to continuous endocytosis and recycling (25). The dileucine motif of MET is required for endocytosis of the receptor, which is mutated to AA in this study (26). First, we have characterized the mutants for endocytosis and degradation. We looked into the degradation kinetics of the mutants by immunoblotting. Unlike the wild-type (WT) MET, the M1250T MET mutant did not undergo degradation upon HGF stimulation (Fig. 3B). Since the M1250T

mutant has a slower degradation rate, we asked whether the M1250T mutant is in its activated form. V5 tagged-MET WT or the mutant was overexpressed and pulled down using Ni-NTA beads through the His-tag present in the coding region. The pulled-down samples were analysed by immunoblotting using the pY-MET antibody. M1250T MET was highly phosphorylated at the active site compared to the WT MET (Fig. 3C). The observation was further confirmed by immunofluorescence. The normalized CTCF value of pY-MET in M120T MET expressing cells was found to be higher compared to WT MET (Fig. S2I). Next, the effect of HGF on the endocytosis of WT or the mutant MET was investigated. Cells were transfected with WT V5-MET or the mutant constructs, and their percentage of localization with EEA1, an early endosomal marker, was quantified in the presence or absence of HGF. HGF stimulation leads to an increased MET population localizing with EEA1 in WT MET expressing cells, whereas M1250T mutant cells showed an increased colocalization with EEA1 irrespective of the HGF stimulation (Fig. 3D, D'). The endocytosis-defective LL/AA mutant did not show any increase in the EEA1 colocalization in response to HGF.

To understand the effect of intracellular trafficking of MET on breast cancer invasion, cells expressing the WT or mutant forms of MET were analyzed for their ECM degradation ability. WT or the mutant V5-MET expressing BT-549 cells were seeded on Alexa568-labeled gelatin-coated coverslip with or without HGF, fixed, and immunostained with anti-V5 antibody. Confocal image analysis showed that WT MET-expressing cells have enhanced ECM degradation ability when stimulated with HGF; however, neither mutant responded to HGF (Fig. 3E, E'). The mutant M1250T MET showed comparable gelatin degradation as the WT MET stimulated with HGF, whereas the LL/AA had decreased invasion ability. We repeated the experiment in MDA-MB-231 cells and observed similar trends for the mutants (Fig. S2J).

Since the ECM degradation ability of M1250T was higher, we asked whether it was because of increased invadopodia formation. M1250T MET-expressing cells showed increased invadopodia formation compared to WT MET-expressing cells (Fig. 3F, S2K, K'). However, cells expressing the LL/AA mutant did not show a significant difference compared to WT MET (Fig. S2K, K'). Also, the number of invadopodia positive for M1250T MET was higher compared to WT MET-positive invadopodia (Fig. 3F)

To further investigate the effect of the M1250T MET mutant on breast cancer invasion, we employed a spheroid invasion assay. We generated a doxycycline-inducible GFP-MET WT and M1250T cell line in BT-549. Spheroids were formed for WT and M1250T MET

expressing cells and embedded in collagen for 24 hours to allow invasion. The M1250T GFP-MET expressing cell line invaded more into the collagen compared to the WT MET expressing spheroid (Fig. 3G), supporting our observations from gelatin degradation.

These observations demonstrated that MET recycling ensures a steady delivery of the RTK to the invadopodia structures, thereby promoting breast cancer invasion.

HGF promotes RAB4 & RAB14-mediated MET delivery to the plasma membrane

RAB GTPases are molecular switches, localized to distinct endosomal compartments, and orchestrate various endocytic, trans, and exocytic pathways (27). To investigate the RABs involved in MET recycling, we first inspected the colocalization of MET with endosomal markers that work in the recycling pathways, like RAB4, RAB22, RAB14 and RAB11. Cells were transfected with the different RAB constructs and incubated in the presence or in the absence of HGF before fixing and immunostaining for MET. The object-based percentage of colocalization was calculated using Motiontracking, for which vesicles for each molecule were identified, and the objects were considered to be colocalized if the overlap of their respective area was more than 35%. While the localization of MET with RAB4 and RAB14 was found to be increased in the HGF-stimulated cells (Fig. 3A-C), the colocalization with RAB22 and RAB11 remained unchanged, suggesting them to be associated with an HGF-independent trafficking pathway (S3A, B).

Next, to identify the RABs that are involved in the HGF-dependent MET surface delivery, live cell TIRF imaging was performed in RAB4, RAB14, and RAB22-depleted cells. As the role of RAB4 in MET recycling has been established before, it was included as a positive control (28). The RABs were silenced using SMARTpool siRNA, and knockdown efficiency was quantified (Fig. S3C). GFP-MET was overexpressed in the control and the RABs-depleted cells and imaged using a TIRF microscope in the presence of HGF. The total number of MET vesicles, including MET tracks at the surface, was found to be reduced when RAB4 or RAB14 was deleted compared to the control cells (Fig. 3D-E, MOVIE 3).

When the recycling is impaired, a significant population of the RTKs is subjected to degradation (25,29). Next, to study the fate of MET in the RABs-depleted cells, we performed immunoblotting to quantify the total population of cellular MET. Cells depleted of the RABs mentioned above were treated with HGF. Cells were lysed and subjected to immunoblotting. The RAB4 and RAB14-depleted cells were observed to have a decreased total MET level compared to the control (Fig. S3D).

Since the retromer is known to drive the recycling of various cargoes to the plasma membrane, we checked the role of retromer depletion on MET recycling (30). The co-localization of MET with VPS35, a retromer subunit, was comparable with or without HGF (Fig. S3E). Further to analyze whether retromer is essential for MET trafficking, MDA-MB-231 cells were depleted for the VPS26A retromer subunit, and the MET localization to Actin at fan-shaped membrane protrusions in response to HGF stimulation was quantified. The membrane pool of MET localizing with actin-rich structures was unchanged in the retromer-depleted condition (Fig. S3F). The total MET in the retromer-silenced cells also remained unaffected (Fig. S3G).

As HGF stimulation leads to increased recruitment of MET to invadopodia, we asked whether RAB4 & RAB14-mediated MET recycling plays a role in invadopodia formation and MET colocalization at the invadopodia. Cells depleted with RAB4 or RAB14 were analyzed for their ability to form invadopodia and the MET localization to the structure. As expected, Invadopodia numbers were reduced in RAB4 and RAB14-depleted cells. Further, MET localization to invadopodia was also found to be reduced (Fig. 4F). In line with previous findings, the number of lamellipodia-forming cells was also drastically reduced in the RAB4 and RAB14-silenced cells (Fig. 4F) (28,29,31).

We examined the colocalization of RAB14 with EEA1, and 60% of the RAB14 was found to be colocalized with EEA1 (Fig. S3I). However, a small population of MET-containing RAB14 vesicles (~10%) was not EEA1 positive and present away from the nucleus. Next, we analyze the distribution of MET to RAB4 and RAB14 vesicles using super-resolution microscopy. The GFP-RAB4 and Cherry-RAB14 expressing cells were stimulated with HGF, then fixed and immunostained for MET. The peripheral vesicles containing MET were positive for RAB4 or RAB14, with RAB14-positive MET endosomes showing minimal or no RAB4 presence, whereas the RAB4-positive MET endosomes are devoid of RAB14 (Fig. S3J).

A study from Wang et.al. suggests that RAB14 vesicles can also be budded out from the Golgi (32). We analyzed the localization with a Golgi marker to understand the biogenesis of these RAB14-MET vesicles. Cherry-RAB14 expressing cells were fixed and immunostained with anti-MET and anti-Golgin97 antibody. A small fraction (4%) of RAB14-positive MET puncta localized with the Golgi (Fig. SK).

When we analyzed the effect of HGF on RAB14 vesicular characteristics. GFP-RAB14 expressing cells were treated with or without HGF, fixed, and imaged with a confocal microscope. The integral intensity and area of RAB14 vesicles were quantified. The area of

GFP-RAB14 vesicles was found to be increased in the HGF-treated cells, whereas the integral intensity was unaffected (Fig. S3H). This indicates that the effect of HGF on the trafficking pathway is not mediated solely by RAB14, but also that additional players are involved in the RAB14-mediated trafficking.

The above results suggest that a fraction of the MET recycles back to the surface via the RAB4 or RAB14-mediated recycling pathway, which is crucial for the recruitment of MET to invadopodia.

RCP-RAB14-KIF16B axis regulates MET trafficking

The mechanism behind HGF-mediated MET recycling through RAB4 has been demonstrated earlier (28,29). So, we set out to study the RAB14-dependent trafficking of MET. RAB coupling protein (RCP) is known to be an interacting partner of RAB14, and a study in the H1299 cell line reported it to interact with MET (33,34). To explore the alterations of RCP in breast cancer, we analyzed 32 publicly available breast cancer datasets consisting of a total of 15404 patients in cBioportal and found that RCP is amplified in these datasets (Fig. S4A). Furthermore, the probability of survival was lower for patients with increased expression of RCP (Fig. S4B).

First, we analyzed the colocalization of MET and GFP-RCP with EEA1. Cells transfected with GFP-RCP were treated with HGF and then fixed, followed by immunostaining for MET and EEA1. In colocalization analysis, we found that 37 % of MET-positive RCP vesicles colocalize with EEA1 (Fig. S4C). To study whether RCP has any role in the RAB14-mediated MET recycling, we examined its subcellular localization on RAB14-MET vesicles in the presence or absence of HGF. Due to the unavailability of a validated antibody for immunocytochemistry for RAB14 and RCP, overexpression constructs were used. The anti-RCP antibody used for immunoblotting was not applicable for immunofluorescence. GFP-RCP and Cherry-RAB14 co-expressing cells were fixed and immunostained for MET. Images were captured using a confocal microscope, and the colocalization of MET-RAB14 with RCP was analyzed. In agreement with Gundry et.al, we observed an increased localization of RCP with RAB14 (35% to 51%) in the presence of HGF stimulation (34). Further, the colocalization of RCP with MET (32% to 48%) and MET-RAB14 (22% to 37%) was found to be increased upon HGF stimulation (Fig. 5A).

Gundry et al. demonstrated that HGF stimulation induces phosphorylation of RCP at Ser435, which enhances its complex formation with RAB14. We analyzed the distribution of MET

and RAB14 in the presence or absence of HGF stimulation with the RCP S435A mutant. An increased colocalization of RCP S435A with MET (38% to 58%) and MET-RAB14 (28% to 48%) vesicles was observed upon HGF stimulation (Fig. S4D). However, the colocalization of RCP S435A with RAB14 did not increase with HGF treatment.

Interestingly, we observed that MET and RCP are enriched at the vesicular buds on RAB14 vesicles (Fig. 5B, S4F), which are critical for cargo sorting and recycling. Live cell imaging of GFP-RAB14 revealed that these buds elongate and undergo fission to form tubulovesicular structures (Fig. 5C, MOVIE 4). Live-cell confocal imaging of cells expressing GFP-RCP and Cherry-RAB14 revealed the presence of RCP in the RAB14 tubules (Fig. 5D, MOVIE 5). Further, fixed cell confocal imaging highlighted that MET is present in these tubular elongations emanating from endosomes along with RCP and RAB14 (Fig. 5E). Further, the MET-containing GFP-RCP vesicles were positive for WASH staining, which promotes actin polymerization at endosomes (Fig. S4G) (35).

To investigate whether RAB14 plays a role in RCP recruitment to MET-endosomes, we overexpressed GFP-RCP in RAB14-depleted cells, then fixed and immunostained them with the anti-MET antibody. Confocal imaging revealed that the percentage of colocalization of MET with RCP was unaltered in the RAB14-silenced cells (Fig. S4E). Next, we examined the role of RCP in RAB14 and MET endosomal association. RCP was depleted with siRNA and validated with qRT-PCR and immunoblotting (Fig. S4H, H'). The cells were transfected with Cherry-RAB14, treated with HGF, and fixed. Further, the cells were immunostained with antibodies against MET and EEA1. Images were captured with a confocal microscope, and colocalization was quantified. A 15% decrease in colocalization of MET to RAB14 endosomes that was present with EEA1 was observed in the RCP-silenced cells compared to the control (Fig. 5F). Further, upon RCP depletion, the colocalization of MET to RAB14 was found to be reduced by 10%, but was statistically non-significant (Fig. 5F). The pool of MET or RAB14 vesicles that do not colocalize with EEA1 as observed in (Fig S3I) was unperturbed upon RCP silencing (Fig. S4I).

Molecular motors are one of the effectors of RAB GTPase, which cause membrane tubulation, thereby promoting protein sorting and trafficking. KIF16B is one of the motor proteins known to work with RAB14 (36). Hence, we analysed the colocalization of MET-containing RAB14 vesicles with KIF16B. Cells expressing YFP-KIF16B and Cherry-RAB14 were fixed and immunostained for MET. Confocal imaging revealed that KIF16B also resides in the

endosomal tubules along with RAB14 and MET (Fig. 5G). Next, we analyzed the colocalization of RAB14-MET endosomes with KIF16B in the presence or absence of HGF. YFP-KIF16B and Cherry-RAB14 co-expressing cells were fixed and immunostained for MET. Images were captured using a confocal microscope, and percentage colocalization was quantified using Motiontracking. An increased colocalization of MET (21% to 43%) and MET-RAB14 (17% to 29%) vesicles with KIF16B was observed in the presence of HGF (Fig. 5H). However, RAB14 colocalization to KIF16B remained unaltered upon HGF treatment (Fig. 5H). Since KIF16B is an effector of RAB14, upon silencing of the GTPase, the colocalization of KIF16B with MET was found to be reduced, as expected (Fig. S4J) (36).

KIF16B is known to promote tubulation in the early endosomes (37). So, to investigate the potential role of KIF16B in RAB14 endosomal tubulations, we overexpressed WT or the dominant negative form of the motor with an Ala substitution at the S109 position of KIF16B. BT-549 cells co-expressing Cherry-RAB14 with WT KIF16B or the S109A mutant were subjected to live cell imaging. In 40% of the WT KIF16B expressing cells, RAB14 tubules were observed, whereas it was only 15% in the case of the S109A mutant expressing cells (Fig. 5I, MOVIE 6). This result suggests a potential role for KIF16B in endosomal tubule formation.

Together, these observations suggest that RCP facilitates the MET colocalization to RAB14 on EEA1 endosomes. Further, RCP, MET, and RAB14 localize to endosomal tubules, which are involved in cargo recycling. Furthermore, the colocalization data suggest that HGF fosters the association of KIF16B to MET-RAB14 vesicles and the motor promotes the RAB14 tubulation, promoting MET trafficking.

HGF-MET facilitates ECM degradation by recycling MT1-MMP to the surface

MT1-MMP is one of the invadopodia-associated surface proteases with a wide range of substrate specificity for diverse ECM components (38). Perturbed MT1-MMP recycling impedes ECM degradation and cancer invasion (7,39). HGF is known to increase the expression and activity of invadopodia-associated metalloproteases MMP2 &MMP9 (40). We asked if HGF-stimulated invadopodia activity is mediated by MT1-MMP. We began by studying the expression of MT1-MMP in HGF-treated conditions. 3h of HGF stimulation did not alter the expression or degradation of MT1-MMP (Fig. S5A, A').

Next, we investigated whether HGF treatment leads to enhanced recycling of the protease. We performed an antibody uptake assay, where cells were incubated with MT1-MMP antibody at

4°C, followed by internalization at 37°C. Antibodies available at the surface were removed, and further cells were incubated with HGF to allow recycling at 37°C. The percent of recycling was calculated as described in the methods. Antibody uptake assay revealed that HGF stimulation induced 30% recycling of antibody-bound MT1-MMP, whereas, in the untreated condition, the recycling of MT1-MMP was 10% (Fig. 6A).

To support our observation from the antibody uptake assay, we employed TIRFM-based imaging to capture MT1-MMP exocytosis in real time. We overexpressed a pH-sensitive GFP, pHluorin-tagged MT1-MMP in MDA-MB-231, and quantified the number of exocytic events using TIRFM. We could see an increased surface delivery of pHluorin MT1-MMP when stimulated with HGF (Fig. 6B, MOVIE 7A, B).

The observation was further validated using surface biotinylation. For biotinylation, untreated or HGF-treated cells were incubated with uncleavable biotin, EZ-linked Sulfo-NHS biotin at 4°C. The cells were lysed, and the biotinylated pool was captured with streptavidin beads. Immunoblot analysis revealed that the HGF-treated cells have a higher surface MT1-MMP pool than the untreated cells (Fig. S5B). CIMPR has been taken as control, whose surface level did not alter with HGF treatment (Fig. S5B').

Next, we asked whether HGF also promotes the endocytosis of MT1-MMP. To address this, an antibody uptake assay was performed in the presence or absence of HGF. Cells grown on coverslips were incubated with MT1-MMP antibody at 4°C for 1h. The cells are allowed to internalize the antibody in the presence or absence of HGF. Cells were fixed, imaged with a confocal microscope, and the integral intensity of the internalized MT1-MMP antibody was quantified. HGF stimulation did not show any effect on the endocytosis of MT1-MMP (Fig. S5D).

MT1-MMP is recruited to Invadopodia for efficient ECM remodelling. Since we saw an increased MT1-MMP recycling to the surface, we investigated the MT1-MMP recruitment to invadopodia in the presence or absence of HGF. MDA-MB-231 was seeded on gelatin with or without HGF. After 6h, cells were fixed and immunostained for invadopodia markers. TIRF imaging revealed that, indeed, HGF treatment leads to more MT1-MMP-containing invadopodia compared to the untreated condition (Fig. 6C). Further, to understand whether the receptor MET is also involved in the MT1-MMP recruitment to invadopodia, MET was silenced using siRNA, and the MT1-MMP population at invadopodia was quantified. Upon

depletion of MET, the number of MT1-MMP-containing invadopodia was reduced (Fig. S5E). However, MET depletion did not alter MT1-MMP expression (Fig. S5C).

Further, to gain insight into the possible role of MET in MT1-MMP recruitment to invadopodia, we examined the localization of MT1-MMP with MET. The percentage of colocalization was increased from 12% to 45% when the cells were stimulated with HGF (Fig. S5F). Super-resolution microscopy revealed that in GFP-MT1-MMP expressing cells, MET localizes to the same endosomal microdomain as MT1-MMP (Fig. 6D). Interestingly, a protein-protein interaction prediction database PSOPIA anticipated the interaction between MT1-MMP and MET (41). To establish the physical interaction between MET and MT1-MMP, we employed a GFP nanobody pulldown approach. Lysates of GFP or GFP-MT1-MMP expressing cells were incubated with GST bead-bound GFP binding protein. The interaction was analyzed by immunoblotting. An increased binding of MET to GFP-MT1-MMP compared to GFP was observed (Fig. 6F). The interaction was supported by performing GFP nanobody pulldown in HeLa and MCF10A DCIS (Fig. S5G). Next, to validate the interaction, we performed a reverse pull-down. We overexpressed GFP or GFP-MT1-MMP with V5-MET. V5-MET was trapped using Ni-NTA beads. Immunoblotting of the pulldown sample revealed that V5-MET exclusively interacts with GFP-MT1-MMP (Fig. S5H).

MT1-MMP is known to cleave and shed the ectodomain of LDL receptor, apo-A1, ApoE, p-selectin, MMP2, MMP13, and αV integrin(42–45). As MT1-MMP and MET interact, we asked whether MT1-MMP can also activate MET by shedding its pro-domain. We quantified the mature MET population of 140 kDa in MT1-MMP-silenced cells by immunoblotting. The total matured MET population remains unchanged in the protease-depleted cells (Fig. S5L). Further, to comprehend the relevance of the interaction between the RTK and MT1-MMP, we hypothesize that their physical association plays a crucial role in their simultaneous enrichment at invadopodia, potentially via co-trafficking. To test this hypothesis, cells were transfected with GFP-MET and Cherry-MT1-MMP and imaged under a TIRF microscope. In live-cell TIRFM, GFP-MET and Cherry-MT1-MMP were found to be co-transported at the cell surface (Fig. 6F, MOVIE 8). These data suggest that HGF promotes MT1-MMP surface delivery and the receptor MET via physical interaction with MT1-MMP, ensuring a directed delivery to invadopodia.

A recent study by Ferrari et.al. suggests that MT1-MMP is not only required for invadopodia maturation but also can affect invadopodia formation (46). To explore the role of MT1-MMP

on invadopodia formation, we analyzed the number of invadopodia formed in the MT1-MMP knocked-out cells. Interestingly, the invadopodia formation was drastically reduced in the MT1-MMP-deleted cells compared to the control, highlighting the significance of MT1-MMP in invadopodia formation (Fig. S5J, J'). Next, the protease was overexpressed, and the number of invadopodia formed was quantified. The overexpression of MT1-MMP WT or a catalytically inactive mutant E240A MT1-MMP increases the invadopodia number; however, no significant change was observed between the E240A MT1-MMP and WT MT1-MMP (Fig. S5K, K'). Since MET can also induce invadopodia formation, we asked whether MT1-MMP can modulate the invadopodia formation ability of MET as a result of their physical interaction. The co-expression of MET WT or M1250T with WT MT1-MMP leads to a 1.8-fold increase in the difference observed in the number of invadopodia formed between the WT and M1250T MET compared to the 1.35-fold increase in overexpression of MET WT and M1250T alone (Fig. 6G). However, E240A MT1-MMP could enhance invadopodia formation up to 1.5-fold in M120T MET expressing cells (Fig. 6G). This highlights the potential influence of MT1-MMP on their invadopodia formation. When we analyzed the MT1-MMP recruitment to invadopodia in the presence of the M1250T mutant, we observed an increased colocalization of MT1-MMP to invadopodia compared to the WT MET (Fig. S5I).

Further, to understand whether the increased invadopodia number in the M1250T MET and MT1-MMP (Fig. 6G) was due to the higher affinity of the MET mutant for MT1-MMP, we employed a pulldown approach. Cell lysates from V5/H-MET WT or M1250T and GFP or GFP-MT1-MMP were incubated with Ni-NTA beads. The pulldown samples were analyzed by immunoblotting. We did not observe a preferential binding of MT1-MMP to M1250T (Fig. S5M), nor was the MT1-MMP expression altered in the mutant expressing cells (Fig. S5N), inferring the increased invadopodia formation of M1250T MET in the presence of MT1-MMP is not because of physical interaction.

Taken together, our observations suggest that the HGF-MET axis directs MT1-MMP to invadopodia. The physical association between MT1-MMP and RTK MET ensures their co-trafficking to the surface, thereby promoting invadopodia formation.

DISCUSSION

Our study elucidates the correlation between MET intracellular trafficking and invadopodia-driven breast cancer invasion. This study highlights that HGF stimulation promotes MET and MT1-MMP recycling to invadopodia. MET and MT1-MMP physically interact, which we

hypothesize to be crucial for their co-trafficking to the cell surface. RAB4 and RAB14 mediate the MET delivery to invadopodia, perturbation of which affects cancer cell invasion. RCP and MET localize to RAB14 endosomal tubules, the formation of which is promoted by KIF16B for efficient MET trafficking.

Invadopodia recruitment of RTKs and its modulation by growth factor stimulation

TKS5 is one of the crucial molecules of invadopodia that act as a scaffold to stabilize and recruit the initial precursor complex to the membrane (47,48). During invadopodium formation, TKS5 intensity gradually increases and stabilizes until the structure is disassembled (22). The current study reveals that MET localizes to around 20% of TKS5-positive invadopodia; however, mature structures are devoid of MET, indicating the temporal association of MET with invadopodia (Fig. 2D, F). The intensity plot of TKS5 versus MET per invadopodium reveals that invadopodia with higher TKS5 intensity showed an inverse correlation of TKS5 with MET fluorescence intensity (Fig. 2E). These observations suggest that MET recruitment and its activity may precede invadopodia maturation (48). Further live cell imaging would confirm the time-dependent recruitment of MET to invadopodia.

The EGF-EGFR axis is known to be involved in the invadopodia formation by activating several molecules associated with invadopodia biogenesis (9). SNARE-mediated delivery of EGFR to invadopodia facilitates EGFR phosphorylation, demonstrating the importance of EGFR trafficking in invadopodia activity (10). Consistent with these studies, we observed that EGF stimulation led to increased recruitment of EGFR to invadopodia, similar to the effect of HGF on MET (Fig. 2G, S2H), presumably due to increased surface delivery. This observation suggests that the growth factor-mediated recruitment of RTKs to invadopodia may be a generalized mechanism applicable to RTKs that are known to promote invadopodia-associated activity.

Regulation of MET trafficking and its implications on cellular behaviour

The RTK signaling begins with growth factor binding to its respective receptor, leading to internalization and subsequent lysosomal degradation. Following receptor internalization, signaling from peripheral endosomes is one of the ways of spatiotemporal regulation of the RTK signaling (49,50). In our study, we have highlighted that HGF can trigger the recycling of MET, in addition to promoting its lysosomal degradation (Fig. 2H, S2F). This HGF-dependent surface delivery of MET leads to its enhanced recruitment to invadopodia (Fig. 2G).

After HGF binding, MET rapidly undergoes endocytosis and enters RAB4-positive endosomes in HeLa cells, from where it gets recycled via GGA3 and CLIP170, further driving cell migration (50,51). Kermorgant et al. further demonstrated that PKCƐ and PKCα facilitate different MET trafficking pathways, promoting cell migration (52,53).

We have investigated the effect of MET trafficking on cancer cell invasion by employing a mutant M1250T MET with a degradation defect, triggering enhanced endocytosis and recycling (25). The mutant showed increased invadopodia formation and invasion ability compared to WT MET (Fig. 3E-G, S2J, K, K'). Further, the mutant MET-expressing cells have increased MT1-MMP-associated invadopodia, suggesting enhanced protease delivery in the presence of the mutant compared to WT MET (Fig. S5I). This confirms the significance of RTK trafficking in invadopodia-associated cancer cell invasion.

RAB14 and its Potential regulators of MET recycling

Our observations underlined the crucial role of RAB4 and RAB14-mediated MET recycling in invadopodia-associated function (Fig. 4D-F). The MET was localized to RAB4 and RAB14 together at the perinuclear compartments; however, the peripheral MET-containing endosomes were distinct for RAB4 and RAB14, suggesting discrete recycling pathways (Fig. S3J).

RAB14 is associated with the recycling of GLUT4, FGFR, MT1-MMP, or E-Cadherin between EE, the Golgi, or the plasma membrane and, in turn, regulates cell migration and invasion (28,33,59,60). RAB-dependent recycling of cargoes relies on Guanine nucleotide exchange factors (GEFs) for their activation. FAM116 is the only GEF known to activate RAB14 (31). Confocal imaging indicated that HGF stimulation leads to an increase in the area of RAB14-positive vesicles without altering the fluorescence intensity (Fig. S3H). This suggests the membrane remodelling of RAB14 vesicles is likely due to vesicle fusion or endosomal membrane remodelling, keeping the GTPase recruitment unaffected. This implies that HGF does not significantly impact the GEF activity for RAB14.

RCP is an interacting partner of RAB14; HGF enhances the RCP–RAB14 interaction by promoting phosphorylation of RCP at S435 (34). Our results showed an increased localization of RAB14 to RCP endosomes in the presence of HGF; however, the phosphorylation-defective mutant of RCP S435 opposed this trend as reported earlier by Gundry et.al. (Fig. 5A, S4D) (34). The RCP S435A mutant shows increased colocalization with MET with HGF stimulation, highlighting that HGF-dependent RCP phosphorylation is important for its

interaction with RAB14 but not for MET. Further, silencing of RCP affected the colocalization of MET with RAB14 at the EEA1-positive compartment (Fig. 5F). However, the peripheral MET-positive RAB14 endosomes, devoid of EEA1, as observed in Fig. S3I, were not affected by RCP depletion (Fig. S4I). The recycling vesicles are usually present near the periphery, so we hypothesize that these vesicles are derived from a distinct RAB14 recycling pathway that is RCP-independent. Similarly, the MET localization to EEA1 was unaffected, conveying that the MET endocytosis is RCP-independent; however, the MET colocalization to RAB14 at the sorting endosome requires RCP. Since RCP directly interacts with MET (33), we speculate that RCP bridges RAB14 and MET through its direct interaction with both molecules, thereby promoting cargo recycling.

RAB14 endosomes are reported to harbour endosomal buds (Fig. 5B, S4F), which serve as a hub for actin remodelling and are critical for selective cargo sorting (32). Confocal live-cell imaging of GFP-RAB14 revealed that the buds elongate to form tubules, to which MET was found to be colocalizing with RCP (Fig. 5C, E, MOVIE 5). RCP and MET also colocalize with WASH (Fig. S4G), signifying the active actin remodelling at these endosomes, which also promotes and stabilizes endosomal tubulation (35). From this, we hypothesize that RCP assists in RAB14-mediated MET trafficking through tubular endosomes.

KIF16B is a plus-end-directed motor known to promote RAB14 vesicle movement (36). KIF16B also regulates the RAB14-dependent MT1-MMP recycling (54). Our data show that HGF stimulation increased the colocalization of KIF16B with MET-containing vesicles in a RAB14-dependent way (Fig. 5H, S4J). We observed that MET and RAB14, harbouring endosomal tubules, also contain KIF16B (Fig. 5G). Literature suggests that motors not only regulate vesicular movement but also help in the formation of endosomal tubules (55–57). A study by Skjeldal et al has previously shown that KIF16B drives tubulation in early endosomes. Our live cell imaging data showed that the dominant negative mutant of KIF16B-expressing cells showed less RAB14 tubulation compared to the WT motor (Fig. 5I, MOVIE 6). This highlights the role of KIF16B in promoting RAB14 endosomal tubulation.

Function of MT1-MMP at invadopodia

MT1-MMP is one of the invadopodia-associated metalloproteases and is overexpressed in TNBC cell lines. Perturbation in MT1-MMP delivery to invadopodia impairs ECM degradation and invasion (7,58). Our observations suggest that the HGF-MET axis promotes MT1-MMP recycling to invadopodia (Fig. 6A-D). We observed that when co-expressed with

WT or catalytically inactive (E240A) MT1-MMP, the MET degradation-defective mutant M1250T MET led to a significant increase in invadopodia formation (Fig. 6G) compared to that in the cells expressing only the MET mutant. Overexpression of the WT or the E240A MT1-MMP led to enhanced invadopodia formation (Fig. S5K). Overall, our results corroborate the earlier report showing a novel catalytically independent role of the protease during the initiation stage of invadopodia formation (46,59). Further molecular dissection of MT1-MMP and MET interaction would be required to understand the functional dependency of MET and MT1-MMP association.

Together, our study provides a mechanistic understanding of the HGF-MET-mediated invadopodia formation and MT1-MMP recycling (Fig. 7). We present evidence demonstrating that MET localization to invadopodia is regulated by RAB4 and RAB14-dependent receptor recycling in response to HGF stimulation. HGF-mediated RCP phosphorylation strengthens its interaction with RAB14. We speculate that, through direct interaction with MET, RCP forms a trafficking-assembly with RAB14 and MET on sorting endosomes. RCP and MET also localize to the endosomal tubules emerging from RAB14 vesicles, representing the trafficking of MET through tubular carriers. KIF16B further gets recruited to the MET-positive endosomes through RAB14 and drives tubulation in RAB14 endosomes. In addition, our data suggests a novel functional interaction between the MET and MT1-MMP, which potentially facilitates the co-transport of MT1-MMP and MET to the invadopodia, driving ECM degradation during TNBC invasion.

Material and Methods

Plasmids, antibodies, and reagents

The following antibodies were purchased commercially: rabbit anti-FISH (TKS5) (SantaCruz, sc-30122), 1:500 (IF), mouse anti-cortactin (Millipore, 05–180), 1:300 (IF); (SantaCruz, sc-55579) 1:500 (IF), rabbit anti-MET (CST, D1C2 XP) 1:400 (IF), 1:1000 (IB), mouse anti-MET (CST, L6E7) 1:500 (IF), 1:1000 (IB), rabbit anti-Phospho-Met (Tyr1234/1235) (CST, D26 XP) 1:800 (IF), 1:1000 (IB), mouse anti-V5 (Sigma, SV5-Pk1) 1:400 (IF), 1:1000 (IB), rabbit anti-Rab11Fip1 (Protein technology, 16778-1-AP) 1:1000 (IB), rabbit anti-mouse MT1-MMP (Millipore, MAB3328), 1:1,000 (IB) and 1:400 (IF); mouse anti-MT1-MMP (R&D Systems,

MAB9181-SP), 1:200 (IF), mouse anti-Vps35(SantaCruz, sc-374372) 1:300 (IF); rabbit anti-Vps26 (Abcam, ab23892) 1:1000 (IB), rabbit anti-EGFR (CST, D38B1), rabbit anti-Golgin97 (CST, D8P2K) 1: 200 (IF); mouse anti-vinculin (Sigma, V9131), 1:1,000 (IB); rabbit anti-actin (Sigma, A2066), 1:1,000 (IB); mouse anti-γ-tubulin (Sigma, T6557), 1:3000 (IB), mouse anti-GFP (Roche, 11814460001), 1:2000 (IB); mouse anti-Rab5 (BD Biosciences, 610724), 1:300 (IF); mouse anti-His (ThermoFischer Scientific), 1:1,000 (IB). The anti-rabbit EEA1 antibody was a kind gift from Professor Marino Zerial (Max Planck Institute of Molecular Cell Biology and Genetics, Dresden, Germany) and was used at 1:1000 (IF). Rabbit anti-WASH antibody was kindly shared by Professor Alexis Gautreau, used at 1:300 (IF).

pLenti MET-GFP (37560) and pCDNA3.1 MET-V5/His (201982) were purchased from Addgene. MET was amplified from pLenti MET-GFP using PCR and cloned into pEGFPN1 vectors using the XhoI and HindIII sites. M1250T and LL/AA mutants were generated in pCDNA3.1 MET-V5/His using site-directed mutagenesis. Primer details are provided in the Table S1. pLVX Tre3G MET-GFP WT was constructed by Mutagenex. pLVX TRE3G MET-GFP M1250T was generated by BIOBOX.

Cell culture

MDA-MB-231 (HTB-26), BT-549 (HTB-122) and HeLa (CCL-2) cell lines were purchased from ATCC and verified to be free of contaminants. MDA-MB-231 cells were maintained in L-15 (Invitrogen) media with 10% FBS, 100 μg ml^{-1} penicillin, and 100 μg ml^{-1} streptomycin at 37°C in CO_2-free conditions. BT-549 cells were maintained in RPMI (Invitrogen) supplemented with 0.023U/ml of Insulin, 10% FBS, 100 μg/ml penicillin, 100 μg/ml streptomycin, at 37°C with 5% CO2. Professor Phillipe Chavrier from the Centre National de la Recherche Scientifique in Paris, France, kindly shared the MCF10A DCIS cell line, which was maintained at 37°C with 5% CO2 in Advanced DMEM-F12 media supplemented with 2 mM glutamine and 5% horse serum (Invitrogen), 100 μg ml^{-1} penicillin, and 100 μg ml^{-1} streptomycin. HeLa cells were cultured using Dulbecco's modified Eagle's medium (DMEM) supplemented with 10% FBS, 100 μg/ml penicillin, 100 μg/ml streptomycin, and 2 mM glutamine, at 37°C with 5% CO2.

Transient transfection and Generation of stable cell lines

50,000 cells per well were seeded on coverslips in 24-well plates one day before the experiment to transfect expression plasmids transiently. Cells were transfected with 0.5 μg of plasmid DNA using LTX/Plus transfection reagent (Life Technologies) for MDA-MB-231 cells and

Lipofectamine 3000 for BT-549 cells. HeLa cells were transfected with polyethylenimine (PEI-1mg/ml), 5µl of PEI /1µg of DNA.

To generate a stable cell line, 2×10^6 cells per ml were seeded in a 35 mm dish and, after 24 h, were transfected with pLVX TRE3G GFP-MET WT or M1250T with pLVX-pEF1a-Tet3G in a 4:1 ratio. Transfected cells were selected using complete media containing 800 µg/ml G418 and 1µg/ml puromycin. The media was changed every third day. Cells that survived antibiotic stress proliferated and formed colonies, were collected, and grown. Each clone was detected for GFP expression by performing immunoblotting and immunofluorescence. After antibiotic selection, cells were maintained in media containing 500 µg/ml G418 and 1µg/ml puromycin. For gene expression, 50-100 ng/ml of Doxycycline was used.

siRNA and shRNA transfection

OntargetPlus siRNA SMARTpool targeting the gene of interest was purchased from Dharmacon. All siRNAs were used at the working concentration of 10–20 nM. The sequences of SMARTpool siRNAs are provided in the Table. S3. Cells were seeded 24 h before performing siRNA transfection. The manufacturer's protocol was used for transfection using Dharmafect as the transfection reagent.

All shRNA clones were part of the MISSION shRNA product line from Sigma-Aldrich. The TRC1.5 pLKO.1-puro non-mammalian shRNA Control Plasmid DNA (SHC002) is a negative control containing a sequence that should not target any known mammalian genes but engage with RISC. Cells were seeded 24 h before performing shRNA transfection. Cells were transfected at 50–60% confluency with 0.5 µg of shRNA plasmid DNA using LTX/Plus transfection reagent (Life Technologies). The sequences for MISSION plasmid shRNAs are provided in the Table. S4.

RNA extraction and quantitative real-time PCR

Total RNA was extracted from the cells using RNAeasy kit (QIAGEN, Cat# 74104), and cDNA was prepared using the High-Capacity RNA-to-cDNA kit (Life Technologies, Cat# 4387406). Real-time qPCR reactions were performed using the SYBR Green Kit and corresponding primers on Applied Biosystems 7300 Real-Time PCR System or Thermo Quant Studio 3.0. The primer details are provided in the Table. S2.

Immunofluorescence and confocal imaging

Cells were fixed in 4% paraformaldehyde (PFA) for 15 min at room temperature. Indirect immunofluorescence was performed on fixed cells. Cells were permeabilized with 0.1% Triton X-100 for 10 min at room temperature, followed by blocking with 5% FBS in 1× PBS. Cells were immunostained with the required primary antibodies, followed by staining with Alexa-labeled secondary antibodies. The coverslips were mounted using Mowiol (Calbiochem, Cat. 475904) on glass slides and imaged using an LSM780 or FV3000 confocal microscope. Data from three independent experiments were subjected to analysis by the automated image analysis program Motiontracking. The cells were randomly selected for imaging. At least 20 images were acquired for each condition in a given experimental setup, and all the images were processed together for quantification.

Object-based colocalization analysis

The objects were identified as vesicles in each channel based on their size, fluorescence intensity, and other parameters by the automated Motiontracking image analysis program. Objects detected in two different channels were considered to be colocalized if the relative overlap of respective areas was >35%. The apparent colocalization value was calculated as the ratio of integral intensities of colocalized objects to the integral intensities of all objects carrying a given marker, and varied from 0.0 to 1.0. The colocalization-by-chance (random colocalization) was estimated by random permutation of object localization in different channels. The apparent colocalization was corrected for random colocalization. Based on this method of calculating colocalization, we thereafter defined multicolor objects as those with a colocalization value greater than 0.35.

CTCF calculation using ImageJ

To calculate Corrected Total cell fluorescence (CTCT) in ImageJ, a cell boundary was drawn. The area, integrated density, and mean gray value of the ROI were calculated by using the "measure" function under "Analyze". To correct the background fluorescence, an ROI of similar size was drawn in the background where no cell is present, and the mean gray value was calculated. The corrected total cell fluorescence (CTCF) was then calculated using the following formula:

CTCF = Integrated density – (Area of the selected cell× Mean fluorescence of the background reading)

Live-cell imaging

Cells were transfected with GFP- and/or mCherry-fused proteins alone or together for 12 h. Cells were trypsinized and seeded on glass-bottom dishes. Cells in complete medium were incubated for 4 h at 37°C in an incubator and further imaged with an Olympus IXplore spinSR microscope with a 100× Plan Apo N objective (oil, 1.42 NA) on an inverted stage equipped with a Tokai Hit onstage incubation system. Images were acquired and analyzed using Motiontracking.

TIRF microscopy and analysis

Live-cell TIRF-M

To specifically capture events occurring near the cell surface, imaging was performed using a Nikon Eclipse Ti2-E inverted microscope equipped with an H-TIRF module and an Okolab on-stage incubation system for temperature and CO_2 regulation. Cells expressing GFP and/or mCherry fusion proteins were seeded on gelatin-coated, glass-bottom dishes containing complete medium. Dual-color imaging was carried out simultaneously using an Apo-TIRF 60× oil DIC N2 objective lens (NA 1.49) and a Nikon LU-N4 laser combiner, with two Orca-Flash4.0 V3 sCMOS cameras (Hamamatsu Photonics). Images were acquired using NIS-Elements AR software version 5.11.00. GFP-tagged proteins were excited using a 488 nm laser, and mCherry-tagged proteins were excited using a 561nm laser.

Calculation of MT1-MMP exocytosis

The movies were imported into the MotionTracking software and processed as described by Goto-Silva et.al. (60). Briefly, to distinguish endosomes from background fluorescence, we applied the Bayesian Foreground/Background Discrimination (BFBD) filter, as implemented in the MotionTracking software (https://Motiontracking.mpi-cbg.de). The BFBD algorithm separates the image intensity into a fast-changing foreground and a slowly changing background, corresponding to moving vesicles and cytoplasmic fluorescence, respectively. This procedure efficiently suppresses the Poisson noise of fluorescence. Since the BFBD attributed the signal from non-moving objects to the background, we sum the previously found foreground and background. Then, a new background estimation was performed as described in Kalaizidis et al. (61) with a window size of 1µm and subtracted from the de-noised images. The images were thresholded by signal-to-noise ratio (SNR) = 2.0, where the amplitude was estimated as signal uncertainty predicted by the BFBD algorithm. The resulting images were segmented by the watershed algorithm. Detected endosomes were associated with the tracks by a dynamic programming algorithm that performs local-in-time/global-in-space optimization

as described in Rink et al. (62). The exocytosis events were preceded by a docking event, which corresponds to immobilization of the endosome and a fast increase of intensity (flash) due to the physics of TIRF microscopy, with consequent total disappearance of the signal. We filtered events with a duration of flash < 4 sec.

Track identification and quantification

MotionTracking was used to identify and analyze vesicles near the cell surface. In the time-lapse movie, fluorescent objects (vesicles) were detected in each frame. Each object was assigned an x-y position, and its fluorescence intensity and size were calculated. Next, objects were linked across consecutive frames to generate tracks, representing the trajectories of individual vesicles over time. Each track was characterized by parameters such as speed, direction, displacement, intensity, and area. To adjust the track break thresholds, the following parameters were considered: total score, area score, intensity score, and integral intensity score. These thresholds were critical for maintaining track accuracy. After optimization of the parameter, the tracks were generated per movie. Each track was considered to represent a vesicle positioned near the plasma membrane.

Fixed-cell TIRF-M

Fixed-cell TIRF-M was performed by plating cells over a gelatin-coated glass-bottom dish, followed by fixation using 4% PFA, and then proceeded for immunostaining. While imaging with a TIRF microscope, the cells were kept in 1×PBS. *Z*-stack images of the fixed samples were acquired with a *z*-step of 0.02 µm. Acquired images were analyzed as maximum intensity projection (MIP) and searched for multicolor objects (as described above) using the automated image analysis program Motiontracking.

Super-resolution microscopy sample preparation

BT549 or MDA-MB-231 cells expressing the protein of interest were fixed in 4% PFA for 15 min at room temperature and then proceeded for indirect immunofluorescence as mentioned above. Image was captured using Zeiss LSM 900 Airyscan or Olympus IXplore spinSR microscope sequentially with laser wavelengths 488 nm and 561 nm. *Z*-stack images of the fixed samples were acquired with a *z*-step of 0.02 µm.

For Airyscan image processing, the Airyscan Joint deconvolution (jDCV) method was used, which uses the Richardson-Lucy algorithm to achieve a resolution up to 90nm.

Gelatin degradation assay

MDA-MB-231, BT549 and MCF10DCIS cells were trypsinized and 50,000 cells were plated on Alexa Fluor 568-labeled fluorescent gelatin for 3-12h. Cells were then fixed and immunostained with DAPI. Images were captured using a Zeiss LSM780 confocal laser scanning microscope with a 40×1.4 NA oil immersion objective or an Olympus FV3000 microscope. Images were processed in the Motiontracking software, where the degradation area was identified as an object, and the degradation index was calculated using the formula

$$\{[(MeanbackgroundIntensit - meanIntensityofthedegradationspots) \div Meanbackgroundintensity] \times \sum Area\ of\ the\ degradation\ spots\} \div Numberofcellsperframe$$

Generation of multicellular spheroids

Spheroids were formed as described previously in Nazari et al. with minor modifications (63). Briefly, non-adherent agarose microwells were generated by pipetting 50μl of pre-warmed 2% w/v agarose solution, made in PBS, into each well of a 96-well plate and allowed to solidify. MDA-MB-231 or BT549 cells were trypsinized, resuspended and 2000 cells were seeded into each well. Plates were centrifuged for 5 min at 100 ×g, 25°C to initiate aggregation of cells within each well. Plates were incubated at 37°C for 2 days to allow cells to grow and form more compact aggregates. For MDA-MB-231, on day 2, 100μl of media was taken out and 100μl of 10% Matrigel (v/v) (Corning, Cat#354277) was added into each well, making the final Matrigel concentration 5%. After brief centrifugation, plates were returned to the incubator and allowed to form compact spheroids for an additional 2 days.

Spheroid invasion into collagen and quantification

The multicellular spheroids were harvested from the microwells and added in the media. Cooled rat tail collagen type I (ThermoFischer Scientific, Cat#A1048301) was neutralized following the manufacturer's protocol to make collagen hydrogels. The spheroids were mixed with the collagen solution for ~ 5 spheroids/ 70μl in a final collagen concentration of 2mg/mL. Next, the solution was added to a 96-well plate and allowed to gel for 30 min at 37°C. 200ul of complete media or Serum serum-free media or serum-free media containing 100ng/ml HGF was added into each well. The spheroids were allowed to invade for 48 hours, and images were captured at Day 0 and after 48 hours using a Nikon Eclipse Ti inverted microscope using the 4× objective at bright field mode. For BT549 GFP-MET WT or M1250T Mutant spheroids,

doxycycline was added to complete media to make a final concentration of 50ng/ml, respectively. Spheroid images were immediately captured at Day 0 with a Nikon Eclipse Ti inverted microscope using a 4× objective at bright field mode. The spheroids were transferred to the incubator and imaged after 24 hours.

The spheroid invasion area was calculated by ImageJ. By color threshold and the wand tracing tool, the core area and the invaded area were identified, the boundary was drawn, and the area was measured. Spheroid invasion was calculated as the ratio of the invaded area to the core area and was plotted. Experiments were performed in triplicate with a minimum of 30 spheroids per condition.

MT1-MMP antibody uptake assay

MDA-MB-231 cells were trypsinized and counted, and 50,000 cells per well were seeded on the gelatin-coated coverslips for 24 h. After the cells had properly adhered and regained their morphology, antibody uptake was performed using anti-MT1-MMP antibody (R&D Systems, MAB9181-SP). Cells were incubated at 4°C with 10 μg ml^{-1} anti-MT1-MMP antibody diluted in serum-free L-15 medium for 1 h. The unbound antibody was removed by washing with 1× PBS. L-15 complete medium was added, and cells were shifted to 37°C to allow internalization of the surface-bound antibody for 30 minutes. Next, an acid wash (0.2 M Acetic acid and 0.5 M NaCl) was given for 4 minutes to remove the surface-bound antibody. Again, the cells were washed with 1× PBS, and complete media was added with or without HGF to allow recycling of the internalized pool. At the required time point, cells were fixed by adding 4% PFA, followed by staining with anti-EEA1 and DAPI.

The % MT1-MMP recycling was calculated using the formula:

$$[(Integal\ intensity\ of\ MT1-MMP\ at\ T_0 - Integral\ intensity\ of\ MT1 - MMP\ at\ T_{10}) \div Integal\ intensity\ of\ MT1-MMP\ at\ T_0] \times 100$$

Western blotting

Cells were harvested and lysed in lysis buffer (50 mM Tris-HCl, pH 7.4, 150 mM NaCl, 2 mM DTT, 1% NP40, and 1 mM EDTA) supplemented with 10 μg ml^{-1} protease inhibitor cocktail (PIC, Sigma). Cell debris was removed by centrifuging at 19,000 ×g for 15 min at 4°C. Protein concentration was estimated using the Bradford assay. Samples were prepared by adding 1× SDS loading dye and boiling at 95°C. Proteins were separated by running on SDS-PAGE, then transferred to a nitrocellulose membrane (0.45 μm; GE Healthcare, Cat. 10600002). The

membrane was blocked with 5% BSA, then incubated for 1 h at room temperature or overnight at 4°C with the respective primary antibody. To detect the bound antibody signal, the membrane was incubated with fluorescently labelled secondary antibody, and protein bands were detected using the Li-Cor Odyssey Infrared Scanning System.

Blot quantification using ImageJ

Densitometric analysis of blot images was performed using ImageJ software. Blot images were saved as 8-bit grayscale files. Using the rectangular selection tool, equal-sized boxes were drawn around each band, and the Gel Analysis function was used to generate intensity profiles. The area under each peak, corresponding to band intensity, was measured after manually defining baselines and subtracting the background signal obtained from a non-band region of the blot. Band intensities were normalized to the corresponding loading control, and relative expression levels were calculated. Quantification was performed on at least three independent experiments, and results are presented as mean ± SD.

MT1-MMP surface biotinylation

To measure the surface population, MDA-MB-231 cells (9×10^4 cells per ml) were grown in a 35-mm plate. After 24h, the cells were treated with or without HGF for 10 minutes at 37°C. Then the culture medium was removed and the cells were washed carefully with 2 ml PBS (6.7 mM $NaHPO_4$, 3.3 mM $NaH2PO_4$, and 140 mM NaCl, pH 7.2) and incubated with EZ-link Sulfo-NHS-Biotin (Invitrogen, Cat. 21217) at 4°C for 45 min. Further, to quench unreacted biotin, cells were treated with a quenching solution (50 mM Tris-HCl, pH 8.0). After quenching, cells were washed with 1× PBS and solubilized in lysis buffer. The lysate was incubated with Neutravidin beads (Pierce, Cat. 29200) for 30 min at room temperature. Biotin-labelled proteins were eluted from the beads and subjected to immunoblotting. The intensity of the biotinylated MT1-MMP was quantified for HGF-treated or untreated samples using ImageJ software. The scanned Western blot image was converted into a grayscale image for densitometric analysis.

GFP-trap pulldown

The GBP clone was purchased from Addgene and subcloned into the pGEX-6P1 vector to express GST-tagged GBP. GFP vector or GFP fusion proteins were overexpressed in the 6-well format. After 16 h of transfection, cells were lysed in 50 mM Tris-HCl, pH 7.4, 150 mM NaCl, 2 mM DTT, 1 mM EDTA, and 1% NP-40, and cleared by centrifuging at 19,000 ×*g* at 4°C for

20 min. Cleared lysates were mixed with 25 µg of purified GST–GBP bound to the glutathione Sepharose beads. The beads bound with GBP–GFP protein complexes were then washed three times with PBS, followed by elution using 1× SDS sample loading buffer. Samples were then separated on an 8% SDS-PAGE gel, followed by Western blotting.

His-Pulldown

Cells expressing proteins of interest were harvested after 16 hours of transient transfection. Cells were lysed in 50 mM Tris-HCl, pH 7.4, 150 mM NaCl, 2 mM DTT, 1 mM EDTA, and 1% NP-40, and cleared by centrifuging at 19,000 ×*g* at 4°C for 20 min. Cleared lysates were incubated with Ni-NTA agarose beads. The beads bound with His tagged protein complexes were then washed three times with PBS, followed by elution using 1× SDS sample loading buffer. Samples were then separated on 8% SDS-PAGE gel followed by Western blotting.

Degradation experiment

Cells were plated for 24 h before the experiment. 50,000 cells per well were seeded in 24-well plates. The next day, cells were treated with HGF in L-15 complete media with cycloheximide at a working concentration of 10 µg ml^{-1}. At different time points, cells were lysed by adding lysis buffer (50 mM Tris-HCl, pH 7.4, 150 mM NaCl, 2 mM DTT, 1% Triton X-100, and 1 mM EDTA) supplemented with PIC. Cell debris was removed by spinning the lysate at 16,000 ×*g* for 15 min at 4°C. Protein estimation was done by Bradford assay, and samples were prepared by adding 1× SDS sample loading buffer and boiling at 95°C. Proteins were separated on an SDS gel and subjected to Western blotting.

PHA665752 or Pervanadate treatment

Cells were treated with a pervanadate/H_2O_2 mixture; for this, 1 ml of a 20 mM sodium orthovanadate stock solution was mixed with 330 µl of 30% H_2O_2 and incubated for 5 min at room temperature, yielding a solution of 6 mM pervanadate plus remaining H_2O_2. To stimulate cells with 40 µM pervanadate/H_2O_2, the prepared solution was diluted 1:5 with H_2O, and 16 µI of this solution was diluted in 2 ml of serum-free L-15 medium, and 500 µl was added to each well containing 3×10^5 cells. As pervanadate/H_2O_2 is unstable, a fresh solution was prepared each time. Cells were treated with pervanadate for 30 min at 37°C. Approximately 20 s before the end of the desired time, cells were pelleted (12,000 ×***g*** for 4 min) and lysed using lysis buffer consisting of 137 mM NaCl, 50 mM Tris-HCl (pH 7.8), 10% (v/v) glycerol, 1 mM sodium orthovanadate, 2 mM EDTA (pH 8.0), 1% vol/vol Nonidet P-40, plus protease

inhibitors leupeptin and aprotinin (10 µg/ml each; Sigma), and 1 mM PMSF. Cell debris was spun down for 15 min at 19,000 ×***g*** at 4°C, and cleared cellular lysates were analyzed by anti-phospho-MET immunoblotting (39).

Statistical analysis

For the statistical evaluation of the datasets from quantitative image analysis, paired or unpaired Student's *t*-test or one-way ANOVA with a Dunnett's multiple comparisons test was performed using GraphPad Prism 6 and 8 software version 6.01 and 8.0.2, respectively. Datasets are presented as Mean±SD or Mean± SEM. For the data that are displayed using SuperPlots, each biological replicate is distinctly color-coded and each dot represents the number of identified multicolor objects in a field of view (frame). One frame comprises 1–3 cells, contributing to a total number of cells (*n*) across the total number of frames acquired. The frame-wise values were separately pooled for each biological replicate to calculate the mean in the SuperPlots, and the SD represents the deviation of the data from these three means (64). The significance is as follows: $P>0.05$, ns (non-significant), $*P\leq0.05$, $**P\leq0.01$, $***P\leq0.001$, and $****P\leq0.0001$. The number of samples, images, and experiments used for quantification is mentioned in the respective figure legends or in figures. In all figures, *n*= number of cells and *N*= number of experiments.

Acknowledgements

We thank Professor Philippe Chavrier [CNRS, Paris, France] for sharing the pCDNA3.1 MT1-MMP pHluorin construct and the MCF10DCIS.com line; Dr. Marc Coppolino for pEGFPN1 Mt1-MMP construct, Professor Marino Zerial (Max Planck Institute, Dresden, Germany) for sharing EEA1 antibody, pEGFP-C1 RAB4 and pEYFP C1 KIF16B construct, Prof. Subba Rao Gangi Setty (IISc, India) for GFPC1 and mCherryC1 RAB14 constructs, Professor Jim.C. Norman (University of Glasgow, UK) and Elizabeth Manning (Vanderbilt University) for pmCherry RCP, pEGFPC2 RCP; Professor Sara Courtneidge for the GFP-TKS5 construct. (Oregon Health & Science University, USA); Professor Luis S. Mayorga (IHEM-CONICET), Mendoza, Argentina, for the GFP-RAB22 construct. We acknowledge Dr. Sameena Parveen for her kind help in generating the MT1-MMP Knock-out cell line, Tanishka and Shaili for helping out with plasmid isolation. We are thankful to the Central Instrumentation Facility at IISER Bhopal, which was used to perform confocal, super-resolution and TIRF microscopy-based experiments. We also acknowledge the FIST facility at IISER Bhopal, supported by the DST, for providing the infrastructure to conduct live-cell imaging-based experiments.

Author contribution

This work was funded by the Science and Engineering Research Board (CRG/2023/000563).
Author contributions: A. Khamari: Conceptualization, data curation, investigation, methodology, visualization, analysis, manuscript writing and editing; A. Guria: investigation, methodology, visualization, analysis; K. Tak: investigation, methodology, analysis; R. Sharma: investigation, methodology, analysis; Y. Kalaidzidis: Motiontracking analysis. S. Datta: Conceptualization, data curation, analysis, funding acquisition, investigation, methodology, project administration, resources, supervision, validation, visualization, and manuscript writing and editing.

Reference

1. Hanahan D. Hallmarks of Cancer: New Dimensions. Cancer Discov. 2022 Jan;12(1):31–46.
2. Pally D, Naba A. Extracellular matrix dynamics: A key regulator of cell migration across length-scales and systems. Curr Opin Cell Biol. 2024 Feb;86:102309.
3. Ferrari R, Infante E, Chavrier P. Nucleus–Invadopodia Duo During Cancer Invasion. Trends Cell Biol. 2019 Feb;29(2):93–6.
4. Eddy RJ, Weidmann MD, Sharma VP, Condeelis JS. Tumor Cell Invadopodia: Invasive Protrusions that Orchestrate Metastasis. Trends Cell Biol. 2017 Aug;27(8):595–607.
5. Linder S, Cervero P, Eddy R, Condeelis J. Mechanisms and roles of podosomes and invadopodia. Nat Rev Mol Cell Biol. 2023 Feb 14;24(2):86–106.
6. Augoff K, Hryniewicz-Jankowska A, Tabola R. Invadopodia: clearing the way for cancer cell invasion. Ann Transl Med. 2020 Jul;8(14):902–902.
7. Sharma P, Parveen S, Vinod Shah L, Mukherjee M, Kalaidzidis Y, Joseph Kozielski A, et al. Title: SNX27-retromer assembly directs MT1-MMP trafficking to invadopodia and promotes breast cancer metastasis.
8. Perrin L, Belova E, Bayarmagnai B, Tüzel E, Gligorijevic B. Invadopodia enable cooperative invasion and metastasis of breast cancer cells. Commun Biol. 2022 Aug 1;5(1):758.
9. Mader CC, Oser M, Magalhaes MAO, Bravo-Cordero JJ, Condeelis J, Koleske AJ, et al. Molecular and Cellular Pathobiology An EGFR-Src-Arg-Cortactin Pathway Mediates Functional Maturation of Invadopodia and Breast Cancer Cell Invasion. Available from: http://cancerres.aacrjournals.org/
10. Williams KC, Coppolino MG. SNARE-dependent interaction of Src, EGFR, and ß1 integrin regulates invadopodia formation and tumor cell invasion. J Cell Sci. 2014;127(8).
11. Rajadurai C V., Havrylov S, Zaoui K, Vaillancourt R, Stuible M, Naujokas M, et al. Met receptor tyrosine kinase signals through a cortactin-Gab1 scaffold complex to mediate invadopodia. J Cell Sci. 2012 Jun 15;125(12):2940–53.

12. Makowiecka A, Simiczyjew A, Nowak D, Mazur AJ. Varying effects of EGF, HGF, and TGFβ on the formation of invadopodia and the invasiveness of melanoma cell lines of different origin. Eur J Histochem. 2016 Dec 9;60(4):2728.

13. Breen L, Gaule PB, Canonici A, Walsh N, Collins DM, Cremona M, et al. Targeting c-Met in triple negative breast cancer: preclinical studies using the c-Met inhibitor, Cpd A. Available from: https://doi.org/10.1007/s10637-020-00937-y

14. Bardelli A, Corso S, Bertotti A, Hobor S, Valtorta E, Siravegna G, et al. Amplification of the *MET* Receptor Drives Resistance to Anti-EGFR Therapies in Colorectal Cancer. Cancer Discov. 2013 Jun 1;3(6):658–73.

15. Mukherjee S, Tessema M, Wandinger-Ness A. Vesicular Trafficking of Tyrosine Kinase Receptors and Associated Proteins in the Regulation of Signaling and Vascular Function. Circ Res. 2006 Mar 31;98(6):743–56.

16. Hoshino D, Branch KM, Weaver AM. Signaling inputs to invadopodia and podosomes. J Cell Sci. 2013 Jul;126(14):2979–89.

17. Pietraszek-Gremplewicz K, Simiczyjew A, Dratkiewicz E, Podgórska M, Styczeń I, Matkowski R, et al. Expression level of EGFR and MET receptors regulates invasiveness of melanoma cells. J Cell Mol Med. 2019 Dec 22;23(12):8453–63.

18. Masuda H, Zhang D, Bartholomeusz C, Doihara H, Hortobagyi GN, Ueno NT. Role of epidermal growth factor receptor in breast cancer. Breast Cancer Res Treat. 2012 Nov 17;136(2):331–45.

19. Ho-Yen CM, Louise Jones J, Kermorgant S. The clinical and functional significance of c-Met in breast cancer: a review. 2015;

20. Ding X, Ji J, Jiang J, Cai Q, Wang C, Shi M, et al. HGF-mediated crosstalk between cancer-associated fibroblasts and MET-unamplified gastric cancer cells activates coordinated tumorigenesis and metastasis. Cell Death Dis. 2018 Sep 1;9(9).

21. Augoff K, Hryniewicz-Jankowska A, Tabola R. Invadopodia: clearing the way for cancer cell invasion. Ann Transl Med. 2020;8(14).

22. Kreider-Letterman G, Castillo A, Mahlandt EK, Goedhart J, Rabino A, Goicoechea S, et al. ARHGAP17 regulates the spatiotemporal activity of Cdc42 at invadopodia. Journal of Cell Biology. 2023 Feb 6;222(2).

23. Baldanzi G, Graziani A. Physiological Signaling and Structure of the HGF Receptor MET. Biomedicines [Internet]. 2015;3:1–31. Available from: www.mdpi.com/journal/biomedicines/

24. Peschard P, Fournier TM, Lamorte L, Naujokas MA, Band H, Langdon WY, et al. Mutation of the c-Cbl TKB Domain Binding Site on the Met Receptor Tyrosine Kinase Converts It into a Transforming Protein. Mol Cell. 2001 Nov;8(5):995–1004.

25. Joffre C, Barrow R, Ménard L, Calleja V, Hart IR, Kermorgant S. A direct role for Met endocytosis in tumorigenesis. Nat Cell Biol. 2011 Jun 5;13(7):827–37.

26. Cho KW, Park JH, Park CW, Lee D, Lee E, Kim DJ, et al. Identification of a pivotal endocytosis motif in c-Met and selective modulation of HGF-dependent aggressiveness of cancer using the 16-mer endocytic peptide. Oncogene. 2013 Feb 21;32(8):1018–29.

27. Bhuin T, Roy JK. Rab proteins: The key regulators of intracellular vesicle transport. Exp Cell Res. 2014 Oct;328(1):1–19.

28. Zaoui K, Duhamel S, Parachoniak CA, Park M. CLIP-170 spatially modulates receptor tyrosine kinase recycling to coordinate cell migration. Traffic. 2019 Mar 15;20(3):187–201.

29. Parachoniak CA, Luo Y, Abella JV, Keen JH, Park M. GGA3 Functions as a Switch to Promote Met Receptor Recycling, Essential for Sustained ERK and Cell Migration. Dev Cell. 2011 Jun;20(6):751–63.

30. Chamberland JP, Ritter B. Retromer revisited: Evolving roles for retromer in endosomal sorting. Journal of Cell Biology. 2017 Nov 6;216(11):3433–6.

31. Linford A, Yoshimura S ichiro, Bastos RN, Langemeyer L, Gerondopoulos A, Rigden DJ, et al. Rab14 and Its Exchange Factor FAM116 Link Endocytic Recycling and Adherens Junction Stability in Migrating Cells. Dev Cell. 2012 May;22(5):952–66.

32. Wang J, Xiong J, Zhang S, Li D, Chu Q, Chang W, et al. Biogenesis of Rab14-positive endosome buds at Golgi–endosome contacts by the RhoBTB3–SHIP164–Vps26B complex. Cell Discov. 2024 Apr 2;10(1):38.

33. Muller PAJ, Trinidad AG, Timpson P, Morton JP, Zanivan S, van den Berghe PVE, et al. Mutant p53 enhances MET trafficking and signalling to drive cell scattering and invasion. Oncogene. 2013 Mar 14;32(10):1252–65.

34. Gundry C, Marco S, Rainero E, Miller B, Dornier E, Mitchell L, et al. Phosphorylation of Rab-coupling protein by LMTK3 controls Rab14-dependent EphA2 trafficking to promote cell:cell repulsion. Nat Commun. 2017 Mar 15;8(1):14646.

35. Simonetti B, Cullen PJ. Actin-dependent endosomal receptor recycling. Vol. 56, Current Opinion in Cell Biology. Elsevier Ltd; 2019. p. 22–33.

36. Ueno H, Huang X, Tanaka Y, Hirokawa N. KIF16B/Rab14 Molecular Motor Complex Is Critical for Early Embryonic Development by Transporting FGF Receptor. Dev Cell. 2011 Jan;20(1):60–71.

37. Skjeldal FM, Strunze S, Bergeland T, Walseng E, FGregers T, Bakke O. The fusion of early endosomes induces molecular motor-driven tubule formation and fission. J Cell Sci. 2012 Jan 1;

38. Sounni NE, Noel A. Membrane type-matrix metalloproteinases and tumor progression. Biochimie. 2005 Mar;87(3–4):329–42.

39. Parveen S, Khamari A, Raju J, Coppolino MG, Datta S. Syntaxin 7 contributes to breast cancer cell invasion by promoting invadopodia formation. J Cell Sci. 2022 Jun 15;135(12).

40. Nabeshima K, Inoue T, Shimao Y, Okada Y, Itoh Y, Seiki M, et al. Front-cell-specific expression of membrane-type 1 matrix metalloproteinase and gelatinase A during cohort migration of colon carcinoma cells induced by hepatocyte growth factor/scatter factor. Cancer Res. 2000 Jul 1;60(13):3364–9.

41. Murakami Y, Mizuguchi K. Homology-based prediction of interactions between proteins using Averaged One-Dependence Estimators. BMC Bioinformatics. 2014 Dec 23;15(1):213.

42. Deryugina EI, Ratnikov B, Monosov E, Postnova TI, DiScipio R, Smith JW, et al. MT1-MMP initiates activation of pro-MMP-2 and integrin alphavbeta3 promotes maturation of MMP-2 in breast carcinoma cells. Exp Cell Res. 2001 Feb 15;263(2):209–23.

43. Xia XD, Alabi A, Wang M, Gu HM, Yang RZ, Wang GQ, et al. Membrane-type I matrix metalloproteinase (MT1-MMP), lipid metabolism, and therapeutic implications. J Mol Cell Biol. 2021 Oct 21;13(7):513–26.

44. Alabi A, Xia XD, Gu HM, Wang F, Deng SJ, Yang N, et al. Membrane type 1 matrix metalloproteinase promotes LDL receptor shedding and accelerates the development of atherosclerosis. Nat Commun. 2021 Mar 25;12(1):1889.

45. Itoh Y. Membrane-type matrix metalloproteinases: Their functions and regulations. Matrix Biology. 2015 May;44–46:207–23.

46. Ferrari R, Martin G, Tagit O, Guichard A, Cambi A, Voituriez R, et al. MT1-MMP directs force-producing proteolytic contacts that drive tumor cell invasion. Nat Commun. 2019 Oct 25;10(1):4886.

47. Felli MP, Gligorijevic B, Daar I, Bailey K, Rosanò L, Masi I, et al. Tumor Cellular and Microenvironmental Cues Controlling Invadopodia Formation. 2020; Available from: www.frontiersin.org

48. Zagryazhskaya-Masson A, Monteiro P, Macé AS, Castagnino A, Ferrari R, Infante E, et al. Intersection of TKS5 and FGD1/CDC42 signaling cascades directs the formation of invadopodia. Journal of Cell Biology. 2020 Sep 7;219(9).

49. Miaczynska M, Pelkmans L, Zerial M. Not just a sink: endosomes in control of signal transduction. Curr Opin Cell Biol. 2004 Aug;16(4):400–6.

50. Barrow-McGee R, Kermorgant S. Met endosomal signalling: In the right place, at the right time. Int J Biochem Cell Biol. 2014 Apr;49:69–74.

51. Ménard L, Parker PJ, Kermorgant S. Receptor tyrosine kinase c-Met controls the cytoskeleton from different endosomes via different pathways. Nat Commun. 2014 May 19;5(1):3907.

52. Kermorgant S, Zicha D, Parker PJ. PKC controls HGF-dependent c-Met traffic, signalling and cell migration. EMBO J. 2004 Sep 29;23(19):3721–34.

53. Ménard L, Parker PJ, Kermorgant S. Receptor tyrosine kinase c-Met controls the cytoskeleton from different endosomes via different pathways. Nat Commun. 2014 May 19;5(1):3907.

54. Hey S, Wiesner C, Barcelona B, Linder S. KIF16B drives MT1-MMP recycling in macrophages and promotes co-invasion of cancer cells. Life Sci Alliance. 2023 Nov 11;6(11):e202302158.

55. van Weering JRT, Sessions RB, Traer CJ, Kloer DP, Bhatia VK, Stamou D, et al. Molecular basis for SNX-BAR-mediated assembly of distinct endosomal sorting tubules. EMBO J. 2012 Nov 28;31(23):4466–80.

56. Chibalina M V., Seaman MNJ, Miller CC, Kendrick-Jones J, Buss F. Myosin VI and its interacting protein LMTK2 regulate tubule formation and transport to the endocytic recycling compartment. J Cell Sci. 2007 Dec 15;120(24):4278–88.

57. Hong Z, Yang Y, Zhang C, Niu Y, Li K, Zhao X, et al. The retromer component SNX6 interacts with dynactin p150Glued and mediates endosome-to-TGN transport. Cell Res. 2009 Dec 24;19(12):1334–49.

58. Frittoli E, Palamidessi A, Marighetti P, Confalonieri S, Bianchi F, Malinverno C, et al. A RAB5/RAB4 recycling circuitry induces a proteolytic invasive program and promotes tumor dissemination. Journal of Cell Biology. 2014;206(2):307–28.

59. Bukhari M, Patel N, Fontana R, Santiago-Medina M, Jiang Y, Li D, et al. Fibroblast activation protein drives tumor metastasis via a protease-independent role in invadopodia stabilization. Cell Rep. 2023 Oct;42(10):113302.

60. Goto-Silva L, McShane MP, Salinas S, Kalaidzidis Y, Schiavo G, Zerial M. Retrograde transport of Akt by a neuronal Rab5-APPL1 endosome. Sci Rep. 2019 Feb 21;9(1):2433.

61. Kalaidzidis Y, Morales-Navarrete H, Kalaidzidis I, Zerial M. Intracellular Background Estimation for Quantitative Fluorescence Microscopy. In: The 39th International Workshop on Bayesian Inference and Maximum Entropy Methods in Science and Engineering. Basel Switzerland: MDPI; 2019. p. 22.

62. Rink J, Ghigo E, Kalaidzidis Y, Zerial M. Rab Conversion as a Mechanism of Progression from Early to Late Endosomes. Cell. 2005 Sep;122(5):735–49.

63. Nazari SS. Generation of 3D Tumor Spheroids with Encapsulating Basement Membranes for Invasion Studies. Curr Protoc Cell Biol. 2020 Jun 21;87(1).

64. Lord SJ, Velle KB, Mullins RD, Fritz-Laylin LK. SuperPlots: Communicating reproducibility and variability in cell biology. Journal of Cell Biology. 2020 Jun 1;219(6).

Fig.1: HGF-induced MET activity promotes TNBC breast cancer invasion through invadopodia-mediated ECM degradation (A) Bright-field images of MDA-MB-231 spheroids embedded in the collagen matrix at 0h and 48h in the presence or absence of HGF or complete media. The ratio of the invaded area to the core area was quantified and plotted. The core has been outlined with green, and the invaded area has been outlined with yellow colour. Data points from individual biological replicates are distinctly color-coded. The error bar represents Mean ±SD, One-way ANOVA with multiple comparisons. **** $P < 0.0001$, * $P < 0.05$, Scale bar: 100µm. N=3, n=30. (B) MDA-MB-231 cells were seeded on Alexa568-labeled gelatin-coated coverslip with or without HGF for 3h. Degradation index was quantified and plotted. The arrowhead represents degradation spots. Data points from individual biological replicates are distinctly color-coded. The error bar represents Mean ±SD, Unpaired t-test, **** $P < 0.0001$. scale bar: 10µm. N=3, n=200. (C) MDA-MB-231 cells were seeded on a gelatin-coated glass-bottom dish and allowed to attach for 3h, followed by incubation with or without HGF for another 3h. Cells were fixed and immunostained for TKS5 and Cortactin. Images were captured using a TIRF microscope. TKS5 puncta positive for Cortactin were considered as invadopodia. Arrowheads indicate TKS5- Cortactin positive puncta. Data points from individual biological replicates are distinctly color-coded. The error bar represents Mean ±SD, Paired t-test, ** $P < 0.01$. scale bar: 10µm. N = 4, n = 150. (D, E) MDA-MB-231 cells were seeded on gelatin-coated coverslips for 3h, followed by incubation

with vehicle or PHA665752 (5 μM) with or without HGF for an additional 3h. Cells were fixed, immunostained with anti-TKS5 antibody, Phalloidin to stain F-actin, and DAPI. Images were captured using a confocal microscope. TKS5 puncta positive for Actin were considered as invadopodia. The inset shows a magnified view of the region indicated by the box. scale bar: 10μm. Inset: 2μm. The error bar represents Mean ±SEM, One-way ANOVA with multiple comparisons. **** $P < 0.0001$, ** $P < 0.01$, ns $P > 0.05$, N=3, n=200. (F) MDA-MB-231 cells were transfected with control SHC002 or MET shRNA clone #3, and after 36h of transfection, cells were seeded on Alexa568-labeled gelatin-coated coverslip for 6h. The cells were fixed and immunostained with anti-MET antibody, Phalloidin, and DAPI. Degradation spots immunostained for Actin were quantified and plotted. The inset shows a magnified view of the region indicated by the box. The Arrowheads indicate the degradation spots that were immunostained for Actin. scale bar: 10μm. Inset: 2μm. The error bar represents Mean ±SEM, Unpaired t-test. *** $P < 0.001$, N=3, n=200.

Fig. S1: HGF-induced MET activity promotes TNBC breast cancer invasion through invadopodia-mediated ECM degradation (A) From the publicly available database cBioportal, various breast tumor datasets were analyzed for the frequency of alterations for MET. Graph showing frequency for different alteration types in the various breast tumor cohorts (B) From the publicly available database cBioportal, various breast tumor datasets were analyzed for the survival of patients with altered EGFR or MET. (C) Immunoblotting of indicated cell lines with MET and Tubulin. (D) Bright-field images of BT-549 spheroids embedded in the collagen matrix at 0h and 48h in the presence or absence of HGF or complete media. The ratio of the invaded area to the core area was quantified and plotted. Data points from individual biological replicates are distinctly color-coded. The error bar represents Mean ±SD, One-way ANOVA with multiple comparisons. scale bar: 100μm. **** $P < 0.0001$, *** $P < 0.001$ N=3, n=30. (E) BT-549 cells were seeded on Alexa568-labeled gelatin-coated coverslip for 3h, followed by incubation with or without HGF for an additional 3h. Cells were fixed, immunostained for TKS5, Cortactin, and imaged with a confocal microscope. The degradation index and number of colocalized TKS5-Cortactin puncta were quantified and plotted. The inset shows a magnified view of the region indicated by the box. The error bar represents Mean ±SEM, Unpaired t-test. scale bar: 10μm. Inset: 2μm, *** $P < 0.001$, ** P <

0.01, N=3, n=200. (F) MCF10A DCIS cells were seeded on Alexa568-labeled gelatin-coated coverslip with or without HGF for 6h. Degradation Index was quantified and plotted. The Arrowhead represents degradation spots. Data points from individual biological replicates are distinctly color-coded. The error bar represents Mean ±SD, Unpaired t-test. scale bar: 10µm. **** P < 0.0001, N=3, n=200. (G) MCF10A DCIS cells were seeded on a gelatin-coated glass-bottom dish for 3h, followed by incubation with or without HGF for 3h. Cells were fixed and immunostained for Cortactin and F-actin. Images were captured using a TIRF microscope. Actin-positive Cortactin puncta were quantified and plotted. The error bar represents Mean ±SEM, Unpaired t-test. scale bar: 10µm. ** P < 0.01, N=3, n=100 (H) MDA-MB-231 cells were seeded on a gelatin-coated glass bottom dish for 3h, followed by incubation with or without EGF stimulation for an additional 3h. Cells were fixed and immunostained for TKS5 and Cortactin. Images were captured using a TIRF microscope. TKS5 puncta positive for Cortactin were considered as invadopodia. The error bar represents Mean ±SD, Unpaired t-test. scale bar: 10µm. **** P < 0.0001, N=3, n=90 (I) MDA-MB-231 cells were transfected with SHC002 control shRNA or 5 shRNA clones against MET. After 48 hours, cells were lysed and subjected to immunoblotting with anti-MET antibody. The numbers indicate the normalized signal intensity of MET. (J) Immunoblot of MDA-MB-231 cell lysate treated with or without HGF in the presence of vehicle or PHA665752, probed for pY1234-35 MET or MET and vinculin.

Fig. 2: Enhanced MET recruitment to Invadopodia upon HGF stimulation

(A) MDA-MB-231 cells were seeded on gelatin-coated imaging dishes for 6h. Cells were fixed and immunostained for Cortactin and MET. Images were captured using a TIRF microscope. Colocalized Cortactin-MET puncta were quantified and plotted. The arrowheads indicate the MET-positive Cortactin puncta. The error bar represents Mean ±SD, scale bar: 10µm, n= 60. (B) GFP-TKS5-expressing MDA-MB-231 cells were seeded on gelatin-coated imaging dishes for 6h. Cells were fixed, immunostained for MET and imaged with TIRFM. The arrowhead indicates the MET-positive TKS5 puncta. scale bar: 10µm. (C) Cherry-TKS5-expressing MDA-MB-231 cells were seeded on gelatin-coated glass-bottom imaging dishes for 6h. Cells were fixed, immunostained with anti-pY-MET antibody and imaged with TIRFM. The arrowhead indicates the pY-MET-positive TKS5 puncta. scale bar: 10µm. (D)

Colocalized TKS5-MET or pY-MET puncta were quantified and plotted. The error bar represents Mean ±SD, N=3, n ≤ 50. (E) The fluorescence intensity of TKS5 and MET at individual invadopodia was quantified using Motiontracking and normalized with their respective mean intensities. The normalized fluorescence intensities of TKS5 (X-axis) and MET (Y-axis) were plotted. The points were fitted with a smoothing spline. n=800. (F) MDA-MB-231 cells were seeded on Alexa568-labeled gelatin-coated coverslips for 12h. Cells were fixed and immunostained for F-actin and MET. The inset shows a magnified view of the region indicated by the box. The white Arrowhead represents Actin at the degradation spots, and the yellow arrowhead represents Actin-MET puncta without degradation. scale bar: 10µm. Inset: 2µm. (G) BT-549 cells were seeded on gelatin-coated coverslips for 3h followed by incubation with or without HGF for 3h. Cells were fixed, immunostained for TKS5, MET and Nucleus. Images were taken using the confocal microscope. Colocalized TKS5-MET puncta were quantified and plotted. The error bar represents Mean ±SEM/SD, Unpaired t-test scale bar: 10µm, *** P < 0.001, N=3, n = 200. (H) BT-549 cells expressing GFP-MET were seeded on glass-bottom dishes. The cells were imaged using a TIRF microscope in the presence or absence of HGF. The GFP-MET vesicles moving in the TIRF field for a minimum of 4 consecutive frames were quantified and plotted as MET tracks. The error bar represents Mean ±SEM, Unpaired t-test. scale bar: 10µm. ** P < 0.01, N=3, n=30.

Fig. S2: HGF promotes MET recycling that drives breast cancer invasion

(A) BT-549 cells were seeded on gelatin-coated coverslips and allowed to adhere for 3h, followed by 3 hours with HGF stimulation. Cells were fixed, immunostained for TKS5, MET, and the Nucleus. Images were captured using the confocal microscope. The inset shows a magnified view of the region indicated by the box. Scale bar: 10µm. Inset: 2µm. (B) The ratio of the integral intensity of MET to TKS5 was calculated, and the frequency distribution was plotted. n= 800 invadopodia. (C) MDA-MB-231 cells were seeded on gelatin-coated glass-bottom dishes in the presence or absence of HGF, after 6h, fixed, and immunostained for TKS5 and MET. The cells were imaged using a TIRF microscope. The percentage of TKS5 puncta positive for MET was quantified and plotted. scale bar: 10µm. Unpaired t-test. *** P < 0.001, N=3, n=120. (D) MDA-MB-231 cells were seeded on gelatin-coated glass coverslips for 3h, followed by incubation with or without HGF for an additional 3h. The cells were fixed and

immunostained with anti-MET, anti-Cortactin antibody, and Phalloidin. The cells were imaged using a confocal microscope. Numbers of Actin-Cortactin puncta positive for MET were quantified and plotted. Scale bar: 10µm. Unpaired t-test. *** $P < 0.001$, N=3, n=200. (E) MDA-MB-231 cells seeded on glass coverslips were stimulated with or without HGF for 2h. Cells were fixed and immunostained for MET and RAB5. The percent colocalization of MET with RAB5 was calculated. scale bar: 10µm. The error bar represents Mean ±SEM. N=3, n=200. (F) MDA-MB-231 cells were treated with HGF for a period of 0-3h in the presence of cycloheximide, lysed at the indicated time points, and subjected to immunoblotting. The numbers represent the relative MET expression at the mentioned time point. (G) BT-549 cells were seeded on gelatin-coated coverslips for 6h and fixed. Cells were immunostained for EGFR, F-actin, and Cortactin. Images were captured with the confocal microscope. scale bar: 10µm. (H) BT-549 cells were seeded on gelatin-coated coverslips for 6h with or without EGF stimulation and fixed. Cells were immunostained for EGFR, F-actin, and Cortactin. Images were captured with the confocal microscope. The percentage of Actin-Cortactin puncta that immunostained for EGFR was quantified and plotted. The inset shows a magnified view of the region indicated by the box. scale bar: 10µm. Inset: 2µm. Unpaired t-test. ** $P < 0.01$, N=3, n=100. (I) WT or M1250T V5-MET expressing BT-549 cells were seeded on glass coverslips cells fixed, and immunostained for V5 and pY-MET. Images were acquired with a confocal microscope. Corrected total cell fluorescence (CTCF) for V5 and pY-MET was calculated using ImageJ. The CTCF of pY-MET was normalized with that of V5 and plotted. scale bar: 10µm. The error bar represents Mean ±SEM, Unpaired t-test. ** $P < 0.01$. N=3, n=10. (J) MDA-MB-231 cells expressing V5-MET WT or mutants were seeded on Alexa568-labeled gelatin-coated coverslips for 12h. Cells were fixed, then immunostained for V5, TKS5, and the Nucleus. Cells were imaged with the confocal microscope. Gelatin degradation by the V5-MET overexpressing cells was calculated. The error bar represents Mean ±SEM, Unpaired t-test. * $P < 0.05$ ns $P > 0.05$ scale bar: 10µm. N=3, n=120 (K, K') V5-MET WT or M1250T or LL/AA mutant expressing MDA-MB-231 cells were seeded on a gelatin-coated glass-bottom dish for 6h and fixed. Cells were immunostained for TKS5, and images were captured with the TIRF microscope. Data points from individual biological replicates are distinctly color-coded. The error bar represents Mean ±SD, Unpaired t-test. Scale. ** $P < 0.01$, ns $P > 0.05$ bar: 10µm. N=3, n=60.

Fig 3: Intracellular trafficking of MET promotes invadopodia-associated ECM degradation and breast cancer cell invasion (A) Graphical representation of WT MET and mutants' endocytosis and degradation. (B) BT-549 cells expressing WT or the mutants of V5-MET were treated with or without HGF for 2 hours, followed by cell lysis. The lysates were subjected to immunoblotting with anti-V5 and anti-vinculin antibodies. The V5 signal intensity was quantified and normalized with Vinculin. Error bar represents Mean ±SEM. Unpaired t-test. * $P < 0.05$. (C) BT-549 cells expressing WT or M1250T V5-MET were lysed and incubated with Ni-NTA beads. The pulled-down samples were processed for immunoblotting for MET and pY-MET. (D, D') WT or mutant V5-MET expressing BT-549 cells were seeded on glass coverslips with or without HGF. Cells were fixed, immunostained for V5 and EEA1. Images were captured with a confocal microscope. V5-MET puncta localizing with EEA1 were quantified and plotted. scale bar: 10µm. The error bar represents Mean ±SEM. ** $P < 0.01$. ns $P > 0.05$ N=3, n=60. (E, E') BT-549 cells expressing V5-MET WT or mutants were seeded on Alexa568-labeled gelatin-coated coverslips with or without HGF for 6h. Cells were fixed, then immunostained for V5 and the Nucleus and imaged with the confocal microscope. Gelatin degradation by the V5-MET overexpressing cells was calculated and plotted. scale bar: 10µm. The error bar represents Mean ±SEM, Unpaired t-test. ** $P < 0.01$, ns $P > 0.05$, N=3, n=120. (F) V5-MET WT or M1250T mutant expressing BT-549 cells were seeded on a gelatin-coated coverslip for 6h and fixed. Cells were immunostained for V5, TKS5, and images were captured with the confocal microscope. The error bar represents Mean ±SEM, Unpaired t-test. scale bar: 10µm. ** $P < 0.01$, N=3, n=120 (G) Bright-field images of GFP-MET WT or M1250T expressing BT-549 spheroids embedded in the collagen matrix at 0h and 24h. The ratio of the invaded area to the core area was quantified and plotted. Data points from individual biological replicates are distinctly color-coded. The error bar represents Mean ±SD, Unpaired t-test. scale bar: 100µm. **** $P < 0.0001$, N=3, n=40.

Fig 4: HGF promotes RAB4 & RAB14 mediated MET delivery to the plasma membrane

MDA-MB-231 cells, seeded on glass coverslips, were transfected with (A) GFP-RAB4 or (B) Cherry-RAB14. After 14h of transfection, cells were incubated for 2h with or without HGF, then fixed and immunostained for MET. Images were captured using a confocal microscope.

scale bar: 10µm. (C) Graph showing the percent colocalization of MET with GFP-RAB4 and Cherry-RAB14 in the presence of absence of HGF treatment. The error bar represents Mean ±SD, One-way ANOVA. ** P< 0.01. N=3, n=200 (D) BT-549 cells were transfected with siRNA against RAB4, RAB14, RAB22, or control siRNA. After 60 hours, cells were transfected with GFP-MET and seeded on the gelatin-coated glass-bottom dish. The GFP-MET-transfected cells were imaged in the presence of HGF using a TIRF microscope for 30 frames without an interval. scale bar: 10µm (E) The GFP-MET vesicles forming the track were identified as mentioned in the Method section. The numbers of GFP-MET tracks moving for at least 4 consecutive frames were quantified for each condition and plotted. In addition, the total number of GFP-MET vesicles was quantified. The error bars represent Mean±SD. Unpaired t-test. *** P< 0.001, ** P< 0.01, ns P > 0.05, N=3, n = 30 (F) BT-549 cells were depleted with RAB4 or RAB14, and after 60h, cells were seeded on gelatin-coated coverslips for 6h with HGF stimulation. Cells were fixed and immunostained for MET, TKS5, and F-actin. Images were captured in a confocal microscope. MET colocalizing with invadopodia was quantified and plotted. The number of cells forming lamellipodia was quantified. scale bar: 10µm. The error bar represents Mean ±SEM, One-way ANOVA, *** P< 0.001, ** P< 0.01. N=3, n=200.

Fig. S3: HGF promotes RAB4 and RAB14-mediated MET delivery to the plasma membrane.

MDA-MB-231 cells seeded on glass coverslips were transfected with (A) GFP-RAB22 or (B) GFP-RAB11. After 14h of transfection, cells were incubated for 2h with or without HGF, then fixed and immunostained for MET. Images were captured using a confocal microscope. The percent colocalization of MET with GFP-RAB22 or GFP-RAB11 in the presence or absence of HGF treatment was calculated and plotted. Scale bar: 10µm. The error bar represents Mean ±SD. Unpaired t-test. ns P > 0.05 N=3, n=200. (C) MDA-MB-231 cells seeded on glass coverslips were incubated for 2h with or without HGF. Cells were fixed and immunostained for MET and VPS35. The percent colocalization of MET with VPS35 was calculated. scale bar: 10µm. The error bar represents Mean ±SEM. Unpaired t-test. ns P> 0.05. N = 3, n = 200 (D). The KD efficiency of RAB4, RAB14, and RAB22 was confirmed by quantitative RT-PCR. N = 3. Values in the graph represent means ± SEM. Paired t-test, ** P < 0.01, * P <

0.05. (E) MDA-MB-231 cells were transfected with control or RAB4, RAB14, or RAB22 siRNA. After 60 hours, cells were harvested and processed for immunoblotting to analyse total MET levels. The relative MET levels were quantified. The numbers indicate the normalized MET signal intensity, N=3. (F) MDA-MB-231 cells were transfected with control or VPS26A siRNA. After 60 hours of transfection, cells were given a pulse of HGF for 5 min, and excess HGF was washed off. The cells were incubated at 37°C for 30 min and fixed. The cells were immunostained for MET and F-actin. Images were captured in a confocal microscope, and MET localized to Actin at the cell periphery was quantified. scale bar: 10µm. The error bar represents Mean ±SD. Unpaired t-test. ns P>0.05. N=3, n=200 (G) MDA-MB-231 cells were transfected with control or VPS26A siRNA. After 60 hours of transfection, cells were harvested and processed for immunoblotting to analyse total MET levels. (H) MDA-MB-231 cells transfected with GFP-RAB14 and incubated with or without HGF. Cells were fixed, immunostained for MET, and then imaged using a confocal microscope. The mean Integral intensity and area of GFP-RAB14 vesicles were calculated and plotted. The error bar represents Mean ±SEM. Unpaired t-test. **** P< 0.0001, ns P>0.05, N=3, n=200. (I) BT549 cells grown on coverslips were transfected with Cherry-RAB14. Cells were treated with HGF for 2h and fixed, followed by immunostaining with antibodies against MET and EEA1. Images were captured using a confocal microscope. The white arrowhead indicate the MET-RAB14-EEA1 positive puncta, yellow arrowhead indicates the MET-RAB14 endosomes devoid of EEA1. scale bar: 10µm. (J) BT-549 cells co-expressing GFP-RAB4 and Cherry-RAB14 were fixed, immunostained for MET and imaged with the super-resolution microscope. The inset shows a magnified view of the region indicated by the box. The white arrowhead represents RAB4-MET vesicles, and the yellow arrowhead represents RAB14-MET vesicles. scale bar: 10µm, Inset: 2µm. (K) BT-549 cells expressing Cherry-RAB14 were fixed, then immunostained with anti-MET and anti-GOLGIN 97 antibodies. Images were captured using the Olympus SpinSR super-resolution microscope. The inset shows a magnified view of the region indicated by the box. scale bar: 10µm, Inset: 2µm.

Fig. 5: RCP-RAB14-KIF16B trafficking axis regulates MET recycling

(A) BT-549 cells seeded on glass coverslips were transfected with GFP-RCP and Cherry-RAB14. After 14h of transfection, cells were incubated for 2h with or without HGF, then fixed

and immunostained for MET. Images were captured using a confocal microscope. scale bar: 10µm. The percent colocalization of GFP-RCP with RAB14 or RAB14-MET in the presence or absence of HGF treatment was calculated and plotted. scale bar: 10µm. The error bar represents Mean ±SD. Paired t-test. * P< 0.05, N=3, n=200. (B) BT-549 cells seeded on glass coverslips were transfected with GFP-RCP and Cherry-RAB14. After 14h of transfection, cells were incubated for 2h with HGF stimulation, then fixed and immunostained for MET. Images were captured using a confocal microscope. The inset shows a magnified view of the region indicated by the box. scale bar: 10µm. Inset: 2µm. (C) BT-549 cells were transfected with GFP-RAB14 and seeded on a glass-bottom imaging dish. Time-lapse images were captured using a confocal microscope. The inset shows the events over time, where the tubule is formed and, upon fission, dissociates from the vesicular body. Scalebar: 10µm, Inset: 2µm (D) BT-549 cells co-transfected with GFP-RCP and Cherry-RAB14 were seeded on a glass-bottom imaging. Time-lapse movies were captured using a confocal microscope. Arrowheads indicate the endosomal tubules containing RCP and RAB14. (E) BT-549 cells seeded on glass coverslips were transfected with GFP-RCP and Cherry-RAB14. After 14h of transfection, cells were incubated for 2h with HGF stimulation, then fixed and immunostained for MET. Images were captured using a confocal microscope. The inset shows a magnified view of the region indicated by the box. scale bar: 10µm, Inset: 2µm. (F) BT-549 cells were treated with control or SMARTpool siRNA against RCP. 60h after transfection, cells were transfected with Cherry-RAB14. After providing 2 hours of HGF stimulation, cells were fixed and immunostained for MET and EEA1. Images were captured using a confocal microscope. The percentage colocalization of RAB14 endosomes containing MET with EEA1 was calculated. scale bar: 10µm. The error bar represents Mean ±SD. Paired t-test. ** P< 0.001, ns P > 0.05, N=3, n=200. (G) BT-549 cells seeded on glass coverslips were transfected with YFP-KIF16B and Cherry-RAB14. After 14h of transfection, cells were incubated for 2h with HGF stimulation, then fixed and immunostained for MET. Images were captured using a confocal microscope. The inset shows a magnified view of the region indicated by the box. scale bar: 10µm, inset: 2µm (H) BT-549 cells seeded on glass coverslips were transfected with YFP-KIF16B and Cherry-RAB14. After 14h of transfection, cells were incubated for 2h with or without HGF, then fixed and immunostained for MET. Images were captured using a confocal microscope. scale bar: 10µm. The percent colocalization of YFP-KIF16B with RAB14 or RAB14-MET in the presence or absence of HGF treatment was calculated and plotted. scale bar: 10µm. The error bar represents Mean ±SD. Unpaired t-test. ** P< 0.01, * P< 0.05, ns P > 0.05, N=3, n=200. (I) BT-549 cells co-transfected with YFP-KIF16B WT or S109A mutant

and Cherry-RAB14 were seeded on a glass-bottom imaging dish. Time-lapse images were captured using a confocal microscope. The inset shows a magnified view of the region indicated by the box. scale bar: 10µm, Inset: 2µm. N=3, n=20.

Fig S4: RCP-RAB14-KIF16B trafficking axis regulates MET recycling

(A) The frequency of alteration of MET in 27 breast cancer datasets was analyzed using the publicly available database cBioportal. The graph shows the frequency of alterations for different breast tumor cohorts. (B) Graph showing the probability of survival of the patients with RCP alteration compared to the unaltered groups. (C) BT-549 cells seeded on glass coverslips were transfected with GFP-RCP. After 14h of transfection, cells were incubated for 2h with HGF stimulation, then fixed and immunostained for MET and EEA1. Images were captured using a confocal microscope. scale bar: 10µm. (D) BT-549 cells seeded on glass coverslips were transfected with GFP-RCP S435A and Cherry-RAB14. After 14h of transfection, cells were incubated for 2h with or without HGF, then fixed and immunostained for MET. Images were captured using a confocal microscope. The percent colocalization of GFP-RCP S435A with RAB14 or RAB14-MET in the presence or absence of HGF treatment was calculated and plotted. scale bar: 10µm. The error bar represents Mean ±SD. Unpaired t-test. ** $P< 0.01$, ns $P > 0.05$ N=3, n=200. (E) BT-549 cells depleted with RAB14 or control siRNA-treated cells were transfected with GFP-RCP for 14 hours, followed by 2 hours of HGF stimulation. Cells were fixed and immunostained for MET and EEA1. Images were captured using a confocal microscope, and the percentage colocalization of RCP with MET was quantified and plotted. The graph represents Mean ±SD. Unpaired t-test. ns $P > 0.05$, N=3, n=200. (F) BT-549 cells seeded on glass coverslips were transfected with GFP-RCP and Cherry-RAB14. After 14h of transfection, cells were incubated for 2h with HGF stimulation, then fixed and immunostained for MET. Images were captured using a confocal microscope. The inset shows a magnified view of the region indicated by the box. scale bar: 10µm. Inset: 2µm. (G) BT-549 cells seeded on glass coverslips were transfected with GFP-RCP. After 14h of transfection, cells were incubated for 2h with HGF stimulation, then fixed and immunostained for MET and WASH. Images were captured using a confocal microscope. scale bar: 10µm. (H, H') BT-549 cells were treated with control or RCP siRNA. The efficiency of gene silencing was estimated by qRT-PCR and immunoblotting. N=2. (I) BT-549 cells were

treated with control or SMARTpool siRNA against RCP. 60h after transfection, cells were transfected with Cherry-RAB14. After providing 2 hours of HGF stimulation, cells were fixed and immunostained for MET and EEA1. Images were captured using a confocal microscope. The percentage colocalization of RAB14 or MET endosomes that do not EEA1 was calculated. scale bar: 10µm. The error bar represents Mean ±SD. Paired t-test, ns $P > 0.05$, N=3, n=200. (J) BT-549 cells depleted of RAB14 or control siRNA-treated cells were transfected with YFP-KIF16B. After 14 hours of transfection, cells were treated with HGF, followed by fixing and immunostaining for MET and EEA1. Images were captured using a confocal microscope, and the percentage colocalization of KIF16B with MET was quantified and plotted. The graph represents Mean ±SD. Unpaired t-test. * $P < 0.05$ N=3, n=200.

Fig. 6: HGF/MET facilitates ECM degradation by recycling MT1-MMP to the surface

(A) MDA-MB-231 cells seeded on coverslips, surface labeled with MT1-MMP antibody at 4°C for 1 h Complete media was added, and cells were shifted to 37°C for 30 minutes to allow endocytosis. To remove surface-bound antibodies, an acid wash was given. After washing with PBS, serum-free media was added with or without HGF, and the cells were shifted to 37°C for 10 minutes to allow recycling from the endocytosed pool. Cells were fixed and immunostained for EEA1. The integral intensity of the MT1-MMP and the percentage of MT1-MMP antibody recycling were calculated. N = 3, n= 300; scale bars = 10 µm. The error bar represents means ± SD. Paired t-test, *** $P< 0.001$, Unpaired t-test, * $P < 0.05$. (B) MDA-MB-231 cells transfected with pHluorin MT1-MMP were seeded on gelatin-coated glass-bottom dishes. Time-lapse imaging was performed in the presence or absence of HGF stimulation using a Nikon TIRF microscope without any intervals for 300 frames. The flashes of pHluorin MT1-MMP, which represent exocytic events, were calculated using Motiontracking. scale bars = 10 µm. The error bar represents Means ± SEM. Unpaired t-test, ** $P < 0.001$. N = 4, n= 35. (C) MDA-MB-231 cells were seeded on gelatin-coated glass-bottom dishes and allowed to attach for 3h, followed by incubation with or without HGF for another 3h. Cells were fixed and immunostained for TKS5, MT1-MMP, and F-actin. Images were captured using a Nikon TIRF microscope. TKS5, MT1-MMP, and Actin-positive structures were identified using Motiontracking. The error bar represents Mean ±SEM, Unpaired t-test, * $P < 0.01$. scale bar: 10µm. N=3, n=120. (D) GFP-MT1-MMP expressing MDA-MB-231 cells were fixed and immunostained for MET. Images were captured using an

LSM900 Airyscan super-resolution microscope. Images were processed using the Airyscan Joint deconvolution (jDCV) method. The image was converted to Maximum Intensity projection for representation. The inset shows a magnified view of the region indicated by the box. Scale bar: 10 µm, inset: 2 µm. (E) GFP or GFP-MT1-MMP expressing BT-549 cells were lysed and incubated with GST agarose beads bound to 25µg of GFP binding protein (GBP). Next washes were given to remove unbound proteins and proceeded for immunoblotting with GFP and MET. WCL: whole-cell lysates (F) MDA-MB-231 cells co-expressing GFP-MET and Cherry MT1-MMP were subjected to live-cell TIRF imaging. The inset represents an event at different time points. Scale bar: 10 µm, Inset: 2 µm. (G) BT-549 cells expressing MT1-MMP WT or a catalytic mutant alone or with V5-MET WT or M1250T mutant were seeded on gelatin-coated coverlips for 6h and fixed. Cells were immunostained for V5 and TKS5. Images were captured with the confocal microscope. The number of TKS5 puncta in the MT1-MMP and/or MET expressing cells was calculated and plotted. The error bar represents Mean ±SD, Unpaired t-test. scale bar: 10µm. ** $P<0.01$, * $P < 0.05$, N=3, n=150

Fig. S5: HGF/MET facilitates ECM degradation by recycling MT1-MMP to the surface.

(A) MDA-MB-231 cells treated with or without 100ng/ml of HGF were lysed and subjected to immunoblotting with anti-MT1-MMP antibody. Vinculin was taken as a loading control. (A') MDA-MB-231 cells treated with 10 µg/ml of cycloheximide in the presence or absence of HGF were lysed and subjected to immunoblotting with anti-MT1-MMP antibody. Tubulin was taken as a loading control. (B, B') Untreated or HGF-treated MDA-MB-231 cells were subjected to surface biotinylation. HGF stimulation was given for 10 minutes, followed by biotin labeling at 4°C for 45 minutes. Washes were given to remove excess biotin; subsequently, biotin was quenched, and cells were lysed. The lysate was allowed to bind with Neutravidin beads, followed by immunoblotting. The numbers indicate the Normalized signal intensity of MT1-MMP. In (B'), the MT1-MMP signal intensity has been normalized with CIMPR. Scale bar: The error bar represents Mean ±SD, Paired t-test, * $P < 0.05$. N=4. (C) MDA-MB-231 cells were treated with control or MET siRNA. The efficiency of gene silencing was estimated by immunoblotting. To analyze total MT1-MMP levels in MET-depleted cells, the membrane was probed with an MT1-MMP antibody. Actin was used as a loading control. (D) MDA-MB-231 cells seeded on coverslips were incubated with MT1-

MMP antibody at 4° C. After PBS washes, cells were shifted to 37° C to allow endocytosis in the presence or absence of HGF. The cells were fixed and immunostained with anti-EEA1 antibody. Images were captured using Zeiss LSM780. The integral intensity of the MT1-MMP antibody was calculated and plotted. Scale bar: 10µm. The error bar represents Mean ±SEM, ns P > 0.05, N=3, n = 200. (E) MDA-MB-231 cells were transfected with control or MET siRNA. After 60 hours of transfection, cells were seeded on a gelatin-coated glass-bottom dish and allowed to attach for 3h, followed by incubation with or without HGF for another 3h. Cells were fixed and immunostained for TKS5, MT1-MMP, and F-actin. Images were captured using a Nikon TIRF microscope. TKS5, MT1-MMP, and Actin-positive structures were identified and plotted. The inset shows a magnified view of the region indicated by the box. The error bar represents Mean ±SEM, Unpaired t-test, *** P < 0.001. scale bar: 10µm. Inset: 2µm. N=3, n=120. (F) MDA-MB-231 cells seeded on glass coverslips were incubated with or without HGF. Cells were fixed and immunostained for MT1-MMP and MET. The percentage colocalization was quantified using Motiontracking. Scale bar: 10µm. The error bar represents Mean ±SD, Unpaired t-test. **** P<0.0001. N=3, n=200. (G) Quantification of GBP pulldown assay of GFP-MT1-MMP in 3 different cell lines. The value represents the signal intensity of trapped MET normalized by pulled-down GFP or GFP-MT1-MMP per assay. GFP and GFP-MT1-MMP bars are represented by distinct colors. (H) GFP or GFP-MT1-MMP and V5/H6-MET co-expressing HeLa cell lysates were incubated with Ni-NTA beads. Washes were given, and the pull-down samples were processed for immunoblotting with anti-GFP and anti-V5 antibodies. WCL: whole-cell lysates. (I) BT-549 cells co-expressing pHluorin MT1-MMP with V5-MET WT or M1250T mutant were seeded on gelatin-coated coverslips for 6h and fixed. Cells were immunostained for V5 and TKS5. Images were captured with the confocal microscope. The number of MT1-MMP puncta localizing with TKS5 was calculated and plotted. The inset shows a magnified view of the region indicated by the box. The error bar represents Mean ±SD, Unpaired t-test. scale bar: 10µm. Inset: 2µm. ** P<0.01, * P < 0.05, N=3, n=100 (J, J') SCR and MT1-MMP knock-out MDA-MB-231 cells were seeded on gelatin-coated glass-bottom dishes for 6 hours. Cells were fixed and immunostained for TKS5 and F-actin. Images were acquired using a TIRF microscope. The number of Actin-TKS5 puncta was quantified and plotted. Scale bar: 10µm. The error bar represents Mean±SD, Unpaired t-test. **** P<0.0001. N=3, n=60. (K, K') BT-549 cells expressing WT or catalytically inactive (E240A) MT1-MMP were seeded on the gelatin-coated glass-bottom dish for 6h, then fixed and immunostained for TKS5. Images were captured using a confocal microscope. The number of TKS5 puncta in MT1-MMP-expressing

cells was quantified and plotted. The error bar represents Mean ±SEM, One-way ANOVA, ** $P < 0.01$, * $P < 0.05$. scale bar: 10µm. N=3, n=150. (L) BT-549 cells coexpressing V5-MET WT or M1250T with GFP or GFP-MT1-MMP were lysed and incubated with Ni-NTA beads. Washes were given to remove unbound proteins. The pulled-down samples were processed for immunoblotting with antibodies against V5 and GFP. (M) BT-549 cells expressing V5-MET WT or M1250T were lysed and subjected to immunoblotting with V5, MT1-MMP, and Actin. (N) MDA-MB-231 cells were treated with control or MT1-MMP siRNA and subjected to immunoblotting. The total level of the mature form of MET with a molecular weight of 140 kDa was analyzed in control and MT1-MMP-depleted conditions. Vinculin was taken as a loading control.

Fig. 7: Proposed model showing RAB14-mediated MET trafficking to invadopodia along with MT1-MMP in the presence of HGF stimulation. HGF stimulation triggers invadopodia formation and ECM degradation by promoting invadopodia formation and MT1-MMP recycling. HGF also increases the recruitment of MET to invadopodia by stimulating the trafficking of the RTK in the RAB4 and RAB14-dependent trafficking pathway. HGF stimulation increases the phosphorylation (34) and colocalization of RCP with MET-containing RAB14 vesicles. RCP and MET are present on the endosomal budding site of RAB14, which further elongate and form tubules. KIF16B gets recruited to these endosomes through RAB14 and drives the endosomal tubulation for efficient cargo trafficking. MT1-MMP interacts with MET, presumably promoting their co-trafficking to invadopodia.

MOVIE 1. **HGF promotes spheroid invasion**

Spheroids were formed using MDA-MB-231 cells and embedded in collagen for 24h. Bright field images of the Spheroids invading into the collagen matrix in the presence or absence of HGF stimulation (Fig. 1A). 1 frame/15mins for 24 hours. Scale bar: 100µm.

MOVIE 2. HGF promotes the surface delivery of MET

BT-549 cells transfected with GFP-MET were seeded on the gelatin-coated glass-bottom dish and imaged using a TIRF microscope for 30s without intervals (Fig. 2H). Scale bar: 10µm, Exposure time (488): 900ms.

MOVIE 3. RAB4 and RAB14 facilitate MET trafficking to the surface

RAB4, RAB14, or RAB22 and control siRNA-treated BT-549 cells were transfected with GFP-MET. The cells were seeded on the gelatin-coated glass-bottom dish and imaged using a TIRF microscope for 30s without intervals. (Fig. 3D-E). Scale bar: 10µm, Exposure time (488): 900ms,

MOVIE 4. GFP-RAB14 endosomes make tubular protrusions

BT-549 cells expressing GFP-RAB14 were seeded on a glass-bottom dish and imaged using a confocal microscope (Fig. 5C). Scale bar: 10µm, Inset: 2µm. Exposure time: 80ms, 1frame/ 0.4s for 1 min

MOVIE 5. RCP and RAB14 localize to the endosomal tubules

BT-549 cells co-expressing GFP-RCP and Cherry-RAB14 were seeded on a glass-bottom dish and imaged using a confocal microscope (Fig. 5D). Scale bar: 10µm, Exposure time: 80ms, 1frame/ 0.4s for 1 min

MOVIE 6. KIF16B promotes RAB14 endosomal tubulation

BT-549 cells co-expressing Cherry-RAB14 with YFP-KIF16B WT or YFP-KIF16B S109A were seeded on a glass-bottom dish and imaged using a confocal microscope (Fig. 5I). Scale bar: 10µm, Exposure time: 80ms, 1frame/ 2.25s for 90sec.

MOVIE 7 (A, B). HGF promotes MT1-MMP surface delivery

MDA-MB-231 cells expressing pH-MT1-MMP were seeded on the gelatin-coated glass-bottom dishes in the presence (7B) or absence of HGF (7A). Time-lapse images were captured using a TIRF microscope without an interval for 300 frames. Scale bar: 10µm, Exposure time: 500ms,

MOVIE 8. MET and MT1-MMP co-traffic at the cell surface

MDA-MB-231 cells co-expressing GFP-MET and Cherry-MT1-MMP were seeded on the gelatin-coated glass-bottom dishes. Time-lapse imaging was done using a TIRF microscope

(Fig. 6F). Scale bar:10μm, Exposure time: 900ms (TIRF 488), 500 (TIRF 568), 1 frame/3s for 30s.

Figure 1

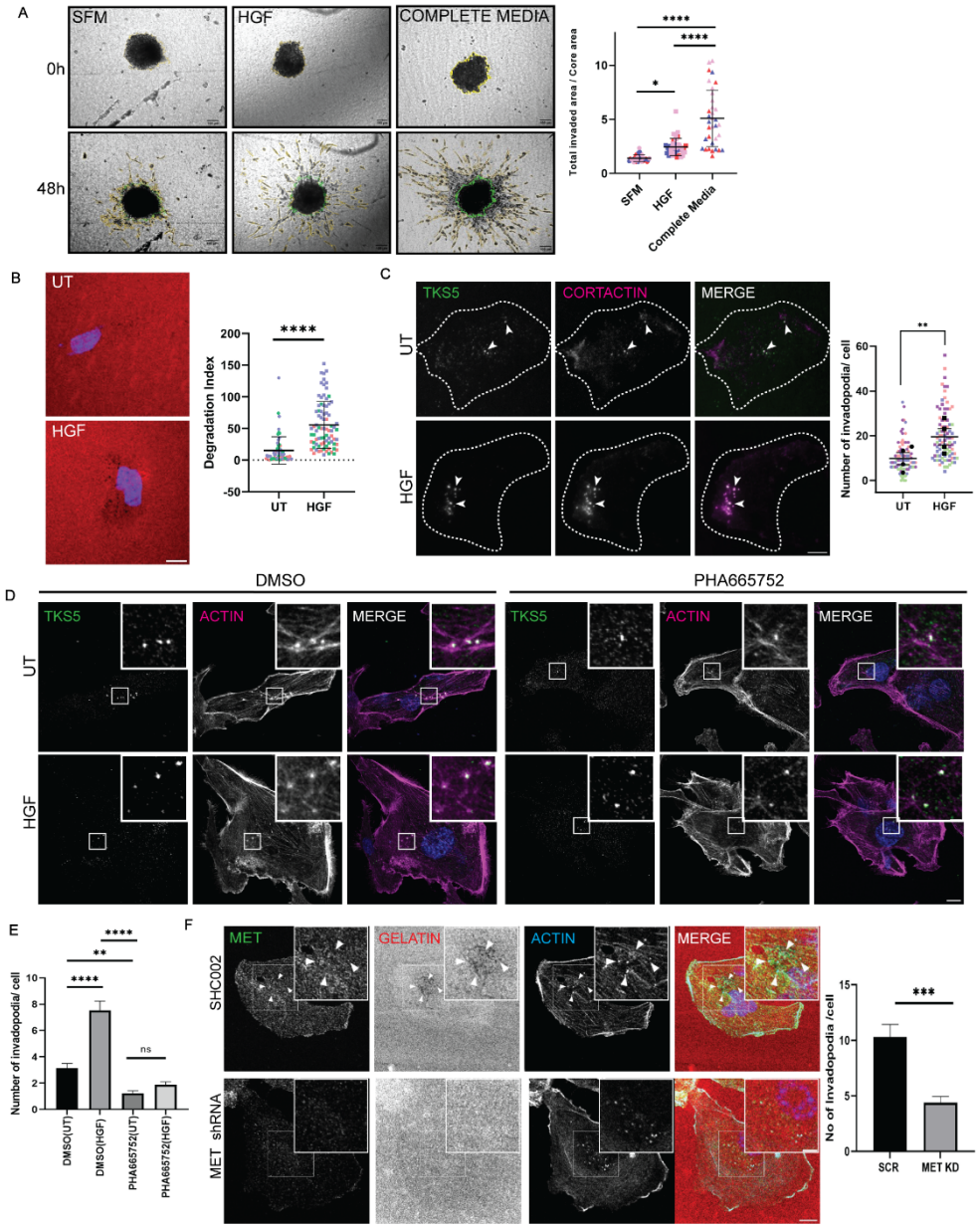
A
SFM
HGF
COMPLETE MEDIA
0h
48h
Total invaded area / Core area
SFM
HGF
Complete Media
B
UT
HGF
Degradation Index
UT
HGF
C
TKS5
CORTACTIN
MERGE
UT
HGF
Number of invadopodia/ cell
UT
HGF
D
DMSO
PHA665752
TKS5
ACTIN
MERGE
UT
HGF
E
Number of invadopodia/ cell
DMSO(UT)
DMSO(HGF)
PHA665752(UT)
PHA665752(HGF)
ns
F
MET
GELATIN
ACTIN
MERGE
SHC002
MET shRNA
No of invadopodia /cell
SCR
MET KD

Figure 2

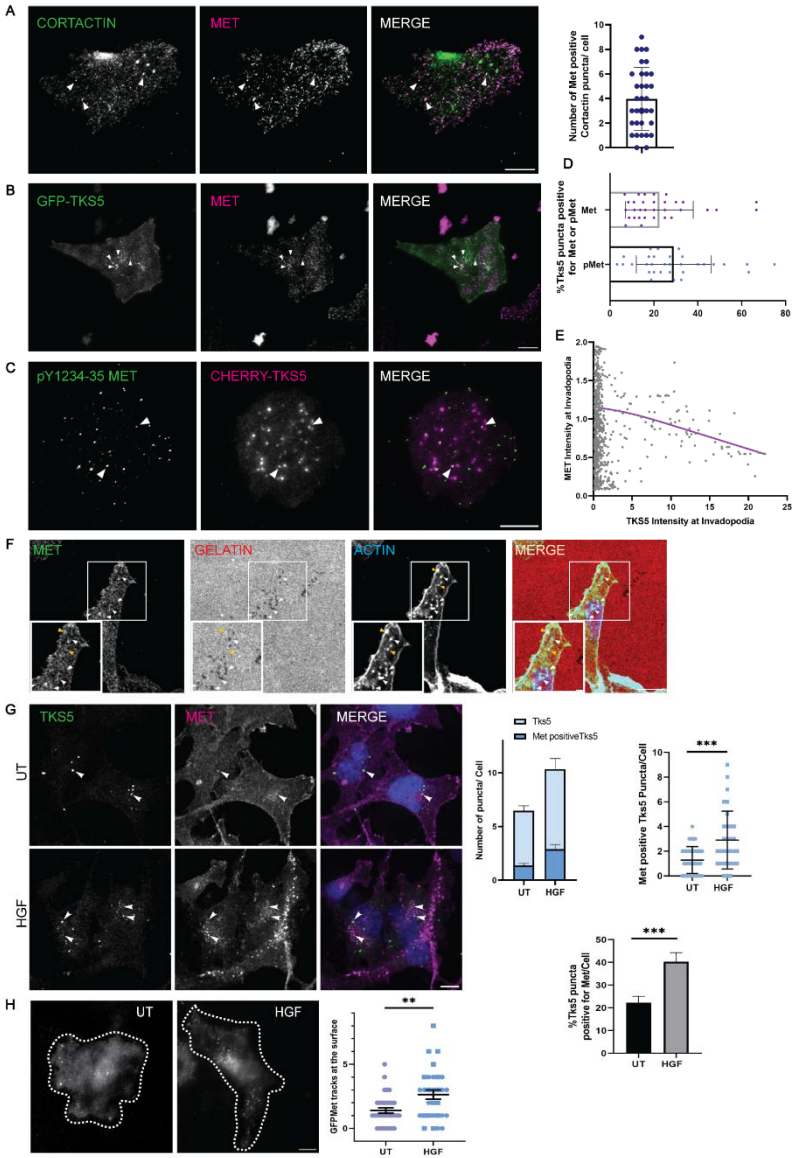
A
CORTACTIN
MET
MERGE
Number of Met positive Cortactin puncta/ cell
B
GFP-TKS5
MET
MERGE
D
% Tks5 puncta positive for Met or pMet
Met
pMet
C
pY1234-35 MET
CHERRY-TKS5
MERGE
E
MET Intensity at Invadopodia
TKS5 Intensity at Invadopodia
F
MET
GELATIN
ACTIN
MERGE
G
TKS5
MET
MERGE
UT
HGF
Tks5
Met positiveTks5
Number of puncta/ Cell
Met positive Tks5 Puncta/Cell
***
% Tks5 puncta positive for Met/Cell
H
UT
HGF
**
GFP/Met tracks at the surface

Figure 3

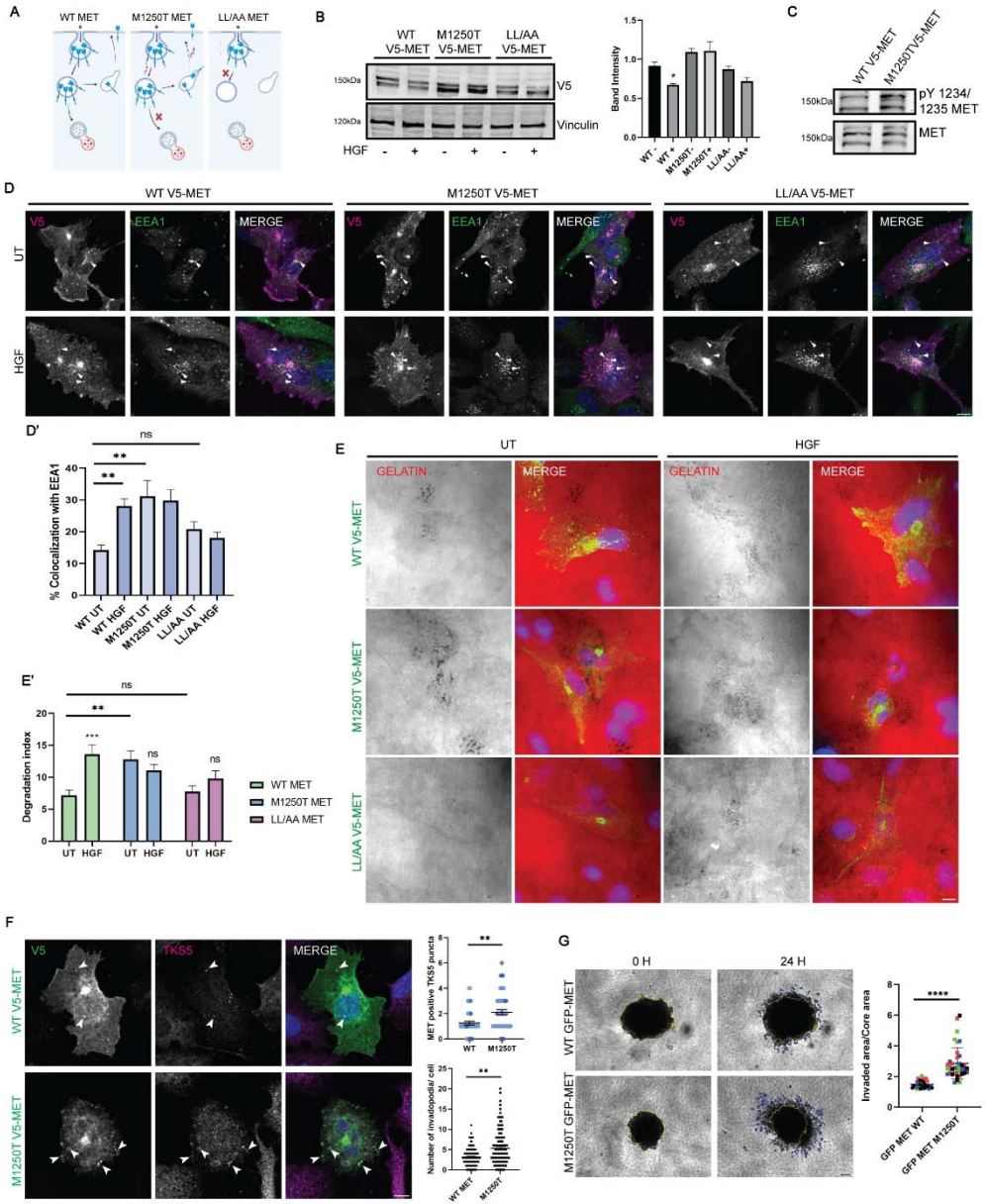
A
WT MET
M1250T MET
LL/AA MET
B
WT V5-MET
M1250T V5-MET
LL/AA V5-MET
150kDa
120kDa
V5
Vinculin
HGF
Band Intensity
C
WT V5-MET
M1250TV5-MET
pY 1234/ 1235 MET
MET
D
WT V5-MET
M1250T V5-MET
LL/AA V5-MET
UT
HGF
V5
EEA1
MERGE
D'
% Colocalization with EEA1
WT UT
WT HGF
M1250T UT
M1250T HGF
LL/AA UT
LL/AA HGF
ns
E
UT
HGF
GELATIN
MERGE
WT V5-MET
M1250T V5-MET
LL/AA V5-MET
E'
Degradation index
WT MET
M1250T MET
LL/AA MET
F
V5
TKS5
MERGE
WT V5-MET
M1250T V5-MET
MET positive TKS5 puncta
Number of invadopodia/ cell
G
0 H
24 H
WT GFP-MET
M1250T GFP-MET
Invaded area/Core area
GFP MET WT
GFP MET M1250T

Figure 4

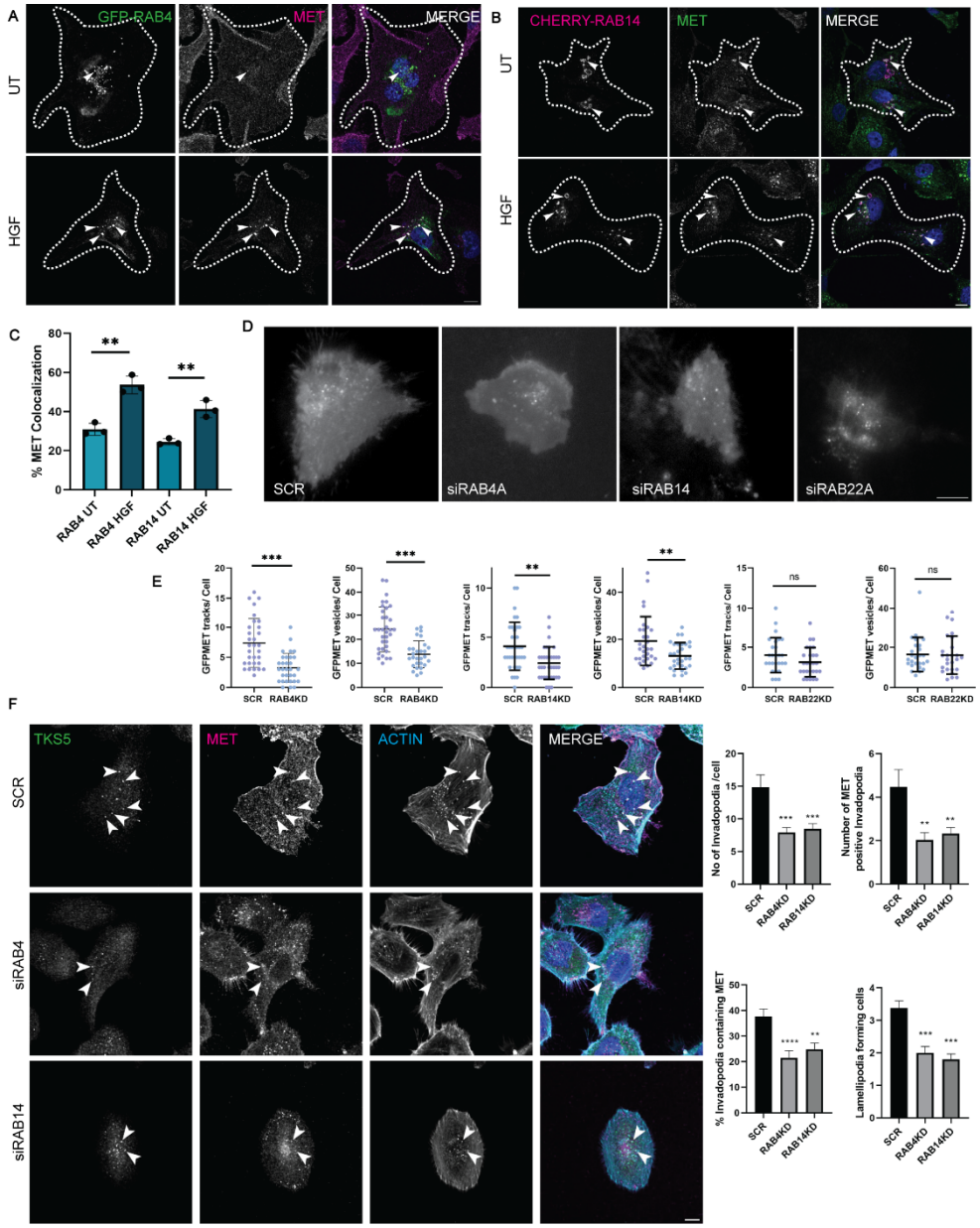
A
GFP-RAB4
MET
MERGE
UT
HGF
B
CHERRY-RAB14
MET
MERGE
UT
HGF
C
% MET Colocalization
RAB4 UT
RAB4 HGF
RAB14 UT
RAB14 HGF
D
SCR
siRAB4A
siRAB14
siRAB22A
E
GFPMET tracks/ Cell
GFPMET vesicles/ Cell
GFPMET tracks/ Cell
GFPMET vesicles/ Cell
GFPMET tracks/ Cell
GFPMET vesicles/ Cell
SCR RAB4KD
SCR RAB4KD
SCR RAB14KD
SCR RAB14KD
SCR RAB22KD
SCR RAB22KD
ns
F
TKS5
MET
ACTIN
MERGE
SCR
siRAB4
siRAB14
No of Invadopodia /cell
Number of MET positive Invadopodia
% Invadopodia containing MET
Lamellipodia forming cells
SCR
RAB4KD
RAB14KD

Figure 5

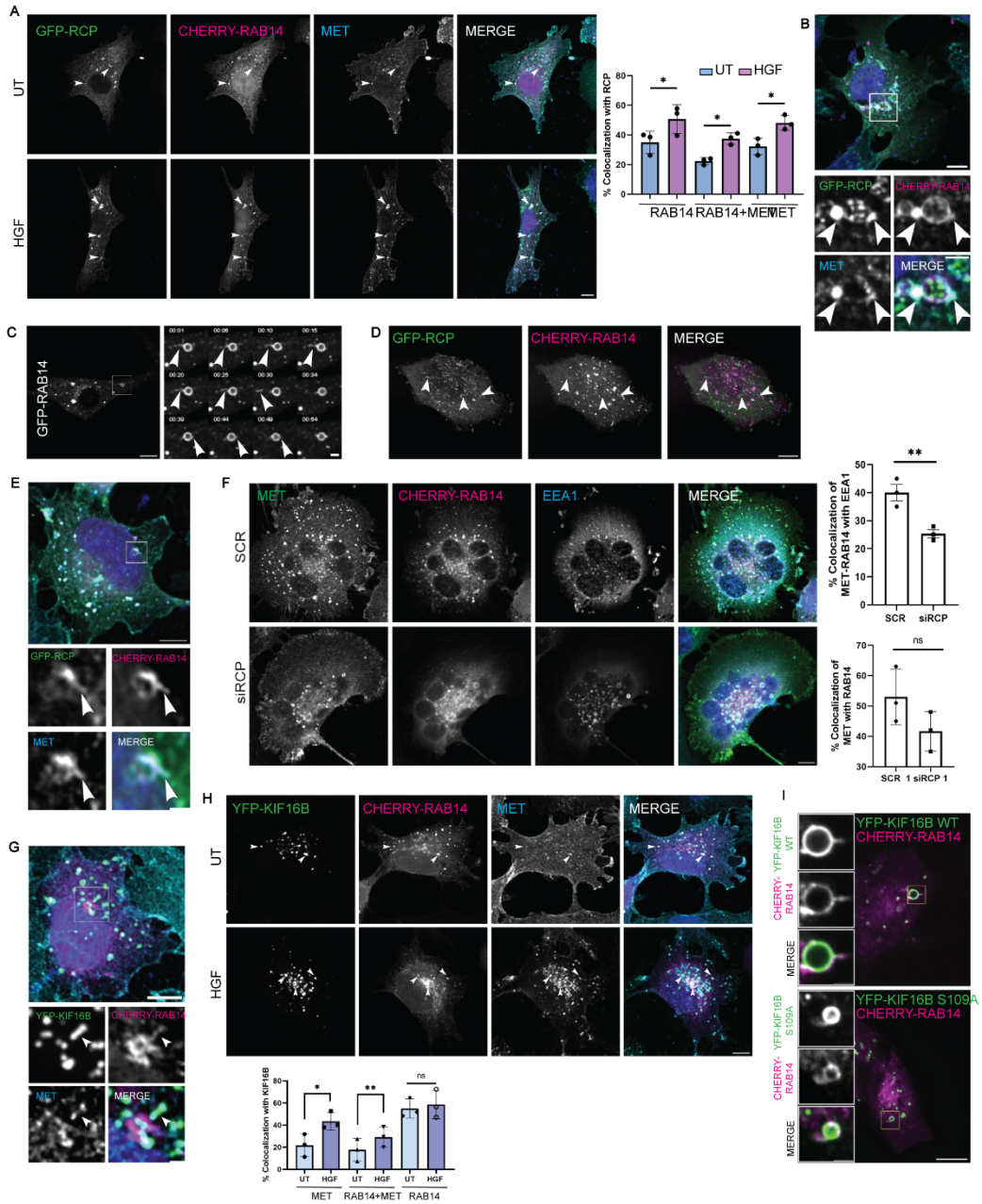
A
GFP-RCP
CHERRY-RAB14
MET
MERGE
UT
HGF
% Colocalization with RCP
UT HGF
RAB14 RAB14+MET MET
B
GFP-RCP
CHERRY-RAB14
MET
MERGE
C
GFP-RAB14
D
GFP-RCP
CHERRY-RAB14
MERGE
E
GFP-RCP
CHERRY-RAB14
MET
MERGE
F
MET
CHERRY-RAB14
EEA1
MERGE
SCR
siRCP
% Colocalization of MET-RAB14 with EEA1
SCR siRCP
% Colocalization of MET with RAB14
SCR 1 siRCP 1
ns
G
YFP-KIF16B
CHERRY-RAB14
MET
MERGE
H
YFP-KIF16B
CHERRY-RAB14
MET
MERGE
UT
HGF
% Colocalization with KIF16B
UT HGF UT HGF UT HGF
MET RAB14+MET RAB14
I
YFP-KIF16B WT
CHERRY-RAB14
YFP-KIF16B S109A
CHERRY-RAB14
MERGE

Figure 6

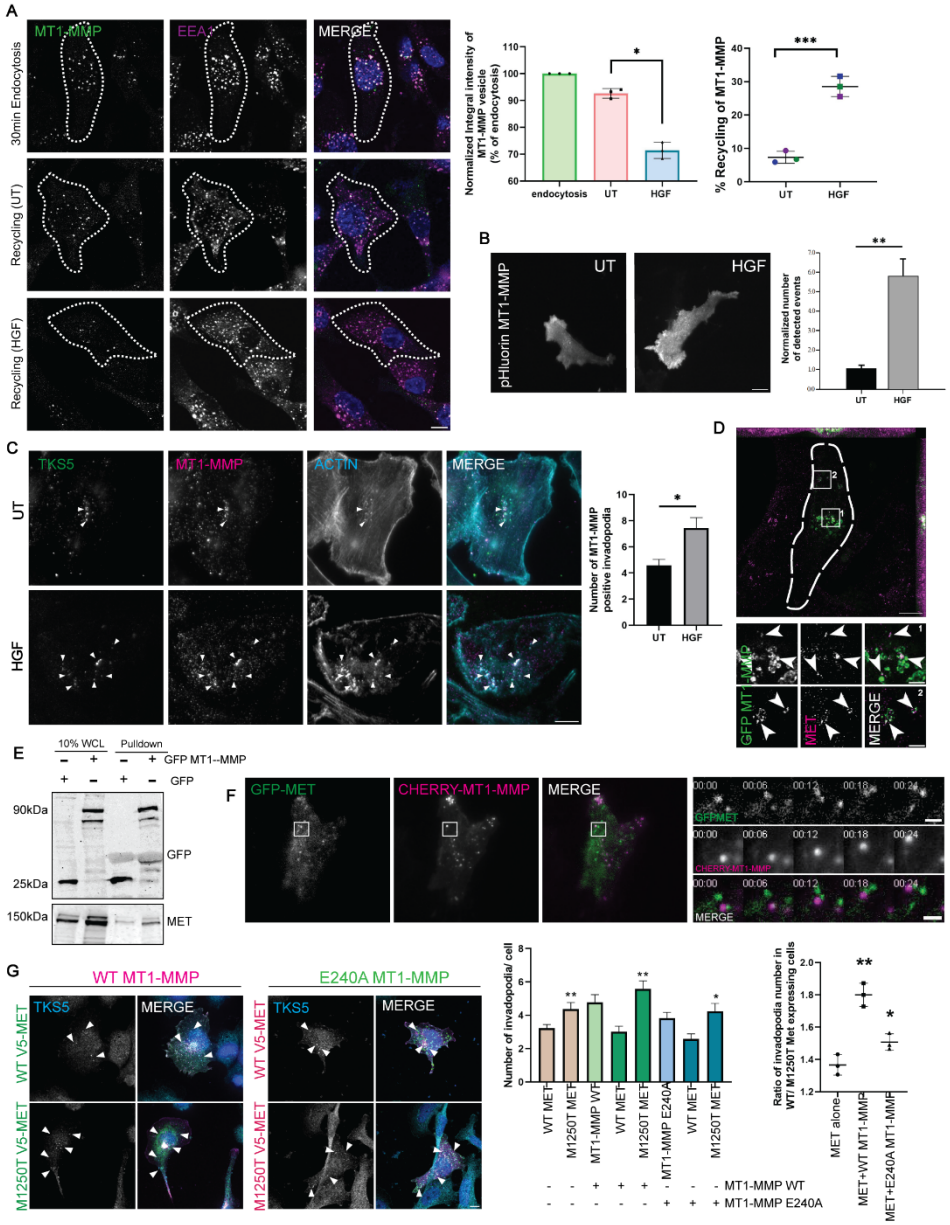
A
MT1-MMP
EEA
MERGE
30min Endocytosis
Recycling (UT)
Recycling (HGF)
Normalized Integral intensity of MT1-MMP vesicles (% of endocytosis)
endocytosis
UT
HGF
% Recycling of MT1-MMP
B
pHluorin MT1-MMP
UT
HGF
Normalized number of detected events
C
TKS5
MT1-MMP
ACTIN
MERGE
UT
HGF
Number of MT1-MMP positive invadopodia
D
GFP MT
MET
MERGE
E
10% WCL
Pulldown
GFP MT1--MMP
GFP
90kDa
25kDa
150kDa
MET
F
GFP-MET
CHERRY-MT1-MMP
MERGE
G
WT MT1-MMP
E240A MT1-MMP
WT V5-MET
M1250T V5-MET
TKS5
MERGE
Number of invadopodial cell
WT MET
M1250T MET
MT1-MMP WT
MT1-MMP E240A
MT1-MMP WT
MT1-MMP E240A
Ratio of invadopodia number in WT M1250T Met expressing cells
MET alone
MET+WT MT1-MMP
MET+E240A MT1-MMP

Figure 7

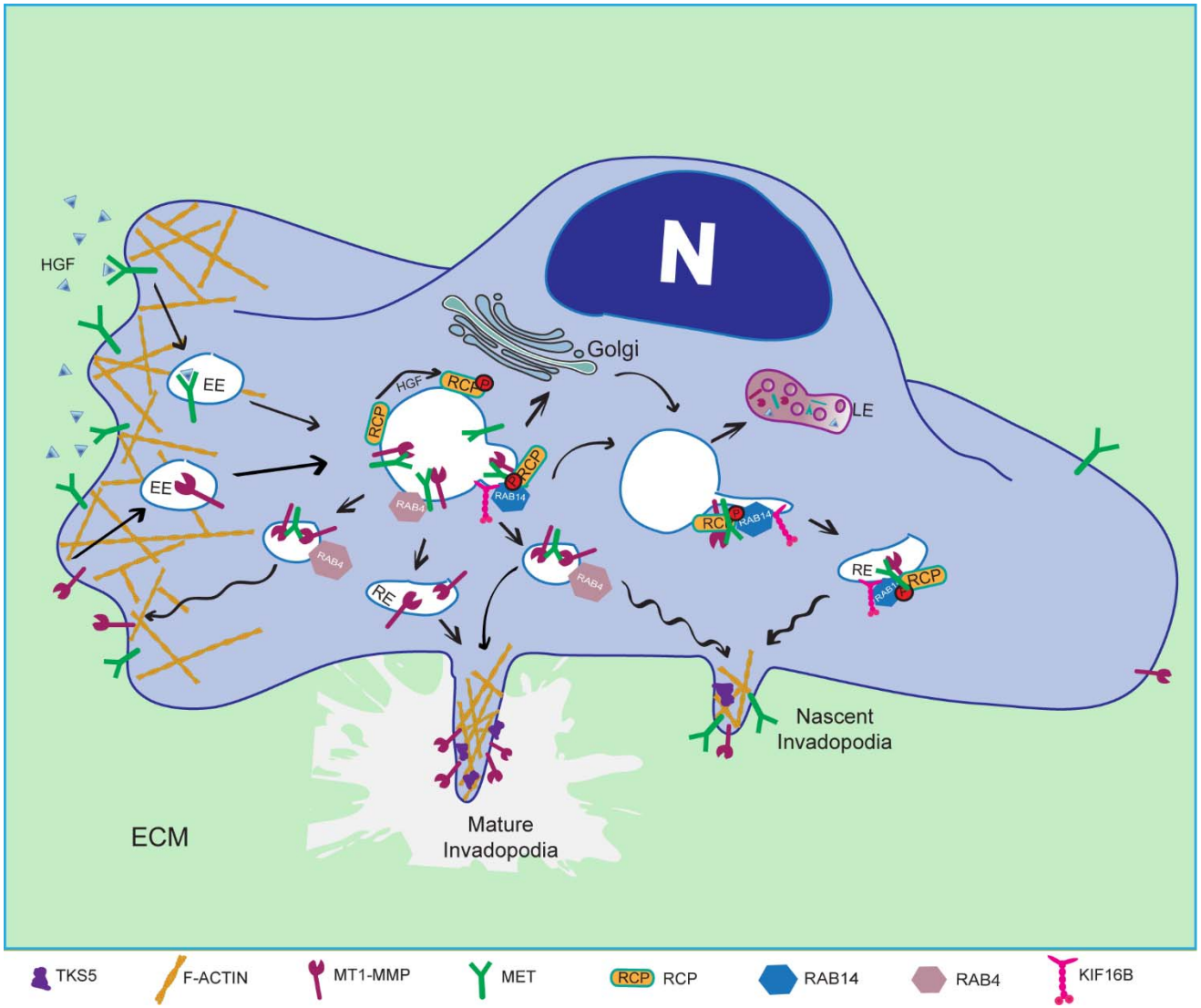
N
Golgi
HGF
EE
EE
HGF
RCP
RCP
RCP
RAB4
RAB14
RAB4
RE
RAB4
LE
RCP
RAB14
RE
RAB14
RCP
Nascent
Invadopodia
Mature
Invadopodia
ECM
TKS5
F-ACTIN
MT1-MMP
MET
RCP
RCP
RAB14
RAB4
KIF16B